Compression of Nanoslit Confined Polymer Solutions

Lili Zeng

A thesis submitted to McGill University in partial fulfillment of the requirements of the degree of **Master of Science**



Department of Physics McGill University Canada, Québec 2018-12-15

© 2018 Lili Zeng All Rights Reserved

Contents

Abstract											
Al	Abrégé Acknowledgements										
A											
St	Statement of Originality and Contribution										
1	Introduction and Motivation										
	1.1	Curren	t State of	Nanofluidics	2						
	1.2	Motiva	ation for S	tudying Polymer Solutions	2						
	1.3	Novelt	y of Curre	ent Work	3						
	1.4	Conce	pt and Out	tline of This Thesis	3						
2	Background										
	2.1	2.1 Theory									
		2.1.1 Single Molecule Under Confinement									
			2.1.1.1	Polymer Physics Formalism	6						
			2.1.1.2	Regimes of Confinement	9						
			2.1.1.3	Above the Overlap Concentration	11						
		2.1.2 Solution Under Confinement									
			2.1.2.1	Self-Consistent Field Approach	13						
			2.1.2.2	Onsager Variational Principle	20						
			2.1.2.3	Rescaling	23						
	2.2	2 Data Analysis Techniques									
		2.2.1 Obtaining Longitudinal Profiles									
			2.2.1.1	Image Processing Procedure	26						

ii CONTENTS

			2.2.1.2	Background Subtraction	27					
		2.2.2	ng Numerical Solutions using FlexPDE	27						
			2.2.2.1	Using Adiabatic Expansion	27					
			2.2.2.2	Using Non-Adiabatic Time Evolution Equation	30					
		2.2.3	Fitting Data to Theory							
			2.2.3.1	Fitting Procedure	31					
			2.2.3.2	Line Spread Function	33					
3	Con	Compression of Nanoslit Confined Polymer Solutions								
	3.1	Preface	e to the M	anuscript	36					
	3.2	2 Abstract								
	3.3	Introduction								
	3.4	Experiment								
	3.5	5 Theory								
		3.5.1	Onsager	's Variational Method Using a Two-Fluid Model	43					
		3.5.2	Reductio	on to One-Dimensional Theory	45					
		3.5.3	Rescalin	g and Numerical Solution	47					
	3.6	Theory	Compare	ed to Experiment	49					
	3.7	Discussion and Conclusions								
	3.8	Supplementary Materials								
4	Con	Conclusion								
	4.1	Summary of Key Results								
	4.2	Outloo	k		60					
Re	eferen	ices			61					

Abstract

How multiple interpenetrating polymer molecules behave in a confined space is a problem of interest both from a biological and a technological standpoint. We probe a solution of DNA molecules confined in a slit-like geometry on a nanofluidics chip. Inside the nanoscale slit, the DNA molecules are compressed via hydrodynamic flow against a barrier permeable only to solvent; the resulting compressed DNA solution concentration profile is recorded as a function of position in the slit. We develop a theoretical model for this concentration profile based on mean-field assumptions and using the Onsager Variational Principle. We find that this model yields a nonlinear Schrödinger type equation governing the concentration profile. We fit this model to our experimental data and we find good agreement for high enough DNA concentration.

Abrégé

Comment multiples molécules de polymère interpénétrantes se comportent dans un espace confiné est un problème d'intérêt d'un point de vue biologique et aussi technologique. Nous étudions une solution de molécules d'ADN confinée dans une lamelle sur une puce nanofluidique. Dans la lamelle de dimensions nanométriques, les molécules d'ADN sont comprimées par un courant hydrodynamique contre une barrière perméable seulement au solvant; le profil de la solution d'ADN comprimée ainsi obtenu est enregistré en fonction de sa position dans la lamelle. Nous développons un model théorique pour ce profil de concentration basé sur l'assomption du champ moyen et utilisant le principe de variation «Onsager». Ce model produit une équation non-linéaire de type «Schrödinger»pour le profil de concentration. Nous ajustons ce model à nos données et trouvons que celles-ci conforment bien à notre prédiction quand la concentration d'ADN est suffisante.

Acknowledgements

First, I am indebted to my supervisor, Prof. Walter Reisner, whose continual support and advice made the completion of my degree possible. His continual belief in me and encouragement are the reason I've made it this far. I have learned from him everything in our trade, from beginning to design a project to completing the final draft of a research paper. He inspires me to become a scientist like him.

I would like to thank Dr. Yue Qi, alongside of whom I've worked for most of my degree, for being a great project partner. I learned much from him and working on our project was that much more enjoyable because of his presence.

I also thank Prof. Reghan Hill for being a counterweight to my supervisor, always offering a different perspective on our project and valuable insight.

I thank the various members of our group who have helped me in various ways: Dr. Susan Amin, Dr. Ahmed Khorshid, Xavier Capaldi, Zezhou Liu, and Dr. Yuning Zhang. I believe I must belong to one of the research groups at McGill with the kindest members.

I also thank my friends, in Montreal and abroad, who have always been there for me: Briah Cahana, Ervin Luka Sešek, Dr. Abeer Barasheed, Daniel Varon, Mercedeh Baroque, and others.

And finally, I can't thank enough my mom and dad. They have been with me through my biggest successes and crises. From financial to emotional support, they would do anything for me. I am so, so grateful.

Statement of Originality and Contribution

This thesis represents the culmination of the work I have done over the past two years of my M.Sc. It has led to the publication of a paper in early 2018 in the journal *Macromolecules* [25] as a coauthor with a postdoc in my research group, Dr. Yue Qi.

Yue designed and fabricated the nanofluidics devices used in the experiments. He also obtained all the experimental data featured in the paper. Yue wrote the first version of the code used to process the raw image data while I wrote the final code used in the paper. I wrote the Matlab and the FlexPDE codes used to compute the numerical solutions to the theoretical model, and fit the data to the numerical solutions. My supervisor Prof. Walter Reisner and I wrote the paper, with Yue contributing in the Experiments section. Yue and I created the figures in the paper. Prof. Reghan Hill provided valuable feedback and editing to the final version of the paper. The entire project was under the supervision and mentorship of my supervisor Walter.

The distinct contributions to scientific knowledge are: (1) the development of an experimental setup to probe the behaviour of confined polymer solutions, (2) the creation of a theoretical model for this behaviour, and (3) the validation of the theoretical model by quantitatively fitting it to our experimental data.

Chapter 1

Introduction and Motivation

1.1 Current State of Nanofluidics

The field of nanofluidics has enabled the manipulation and sensing of single or multiple polymer molecules with applications ranging from simulating biological environment to DNA nanochannel mapping and nanopore sequencing. The development of nanofluidics has led to efforts at studying the physics of polymers in confinement, in order to understand the behaviour of the manipulated polymers and improve device design. Molecules like DNA can mould themselves into the shape of the devices that confine them: they extend themselves in nanochannels [26] and compact themselves when pushed into nanopits [3, 21]. The equilibrium behaviour of single polymer molecules under confinement (0D, 1D or 2D) is now well understood, with for each type of confinement many confinement regimes each with its own scaling relationships [26, 30, 6]. Even non-equilibrium single-chain systems [17, 18] and single-chains in complex confinement geometries [21] have been studied and characterized. However, multi-chain systems under confinement are still poorly understood.

1.2 Motivation for Studying Polymer Solutions

From the point of view of nanofluidics, understanding the physics of polymer solutions under confinement is as fundamental as understanding the physics of single chains under confinement. We need to know how polymer solutions flow and compress in micro/nanosized channels or slits in order to design better devices that manipulate polymer solutions. Even with devices that are designed to sense or manipulate single molecules, there can be regions in the device corresponding to a sudden change of geometry where molecules can build up and form a concentrated local solution. For instance, this could happen at the entrance of a nanochannel [39], at the interface of an entropic trap and a nanochannel [13], or at the entrance of a nanopore [38]. It is therefore important to know the behaviour of polymer solutions to avoid "clogging" in these places.

From the point of view of biology, an ultimate goal is to understand the behaviour of biological multi-chain systems, such as the multiple chromosomes in the nucleus of an eukaryotic cell. Probing an *in vitro* multi-chain system is the first step to understanding how *in vivo* multi-chain systems behave [2].

1.3 Novelty of Current Work

The physics of single chains is now well understood, and if a multi-chain system is dilute enough such that the molecules don't overlap each other, such a system behaves like single chains. However, different behaviours arise once the multi-chain system reaches semidilute concentration where the molecules do overlap. De Gennes first studied confined semidilute flexible polymer solutions [6] and his theory has been tested in simulations [35] and experiments in porous media [22], but not in rigorously defined nanofluidics systems. Moreover, DNA is a semiflexible molecule, with a persistence length around 50 nm, which is much larger than its width of around 2 nm [26]. Sakaue has shown that for the single molecule case, introducing semiflexibility leads to different confinement regimes than those described by de Gennes [16, 31]. For semiflexible molecules, mean-field scalings can be exact (these regimes are called "marginal solution regimes" in classical solution theory [1, 32]) whereas for flexible molecules, concentration fluctuations have a non-negligible effect on scaling exponents. Therefore, the question is whether semiflexible polymer solutions exhibit mean-field or flexible behaviour. Answering this question experimentally would be a first step towards understanding semiflexible polymer solutions. Previous studies in our group demonstrate that single DNA molecules compressed in a nanochannel using a sliding piston exhibit mean-field behaviour [17, 18]. The present thesis would be a natural extension of this work by studying its multi-chain equivalent. A final note is that non-equilibrium behaviour of polymers under confinement is only beginning to be studied [17, 18]. It is all the more important to study the nonequilibrium behaviour of polymer solutions experimentally because polymer solutions are more computationally intensive to study in simulations than single molecules [14].

1.4 Concept and Outline of This Thesis

In this thesis, we develop a nanofluidic device to study polymer solutions in slit-like confinement, analogous to devices used to manipulate single molecules. Multiple DNA molecules are introduced in a nanoslit during an experiment, and solvent flow is applied to push the DNA against a barrier at the end of the slit that is permeable to solvent but not to DNA molecules, as shown in Fig. 1.1(a). The degree of compression of DNA can be tuned by varying the solvent flow speed. The build-up of DNA against the barrier, which exists as a non-equilibrium steady-state, is imaged (Fig. 1.1(b)) and converted to our key observable: a one-dimensional DNA concentration as a function of distance from the slit barrier (Fig. 1.1(c)). We show that this concentration profile can be described by a mean-field type theory based on M. Doi's two-fluid model [10] and the Onsager variational

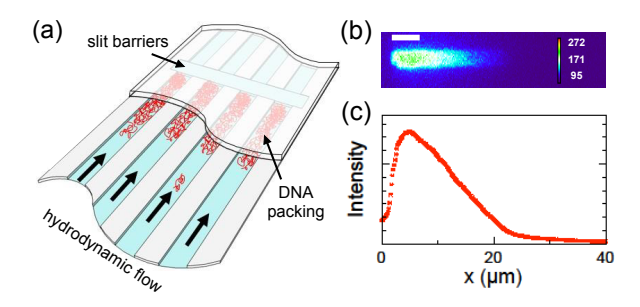


Figure 1.1: (a) Schematic showing dense packing of DNA against a slit barrier inside an array of nanoslits. (b) Full two-dimensional intensity profile for 79 ± 6 DNA molecules, with an applied pressure of 27 mbar (corresponding to a flow speed of $1.13 \,\mu\text{m/s}$). The slit barrier is on the left end of the figure. Scale bar indicates $5 \,\mu\text{m}$. (c) One-dimensional fluorescence intensity profile along the channel axis extracted for the same data set.

principle [8], if the number of DNA molecules, or packing concentration, is high enough.

This thesis is a manuscript-based thesis; the manuscript was published in the journal *Macro-molecules* in 2018 [25]. The first section provides the background information, including a theory and a data analysis techniques overview, to support the content inside the manuscript. The second section is the manuscript itself, with the last subsection acting as a footnote for details omitted in the manuscript itself. The thesis ends with a conclusion which introduces future projects in our group.

Chapter 2

Background

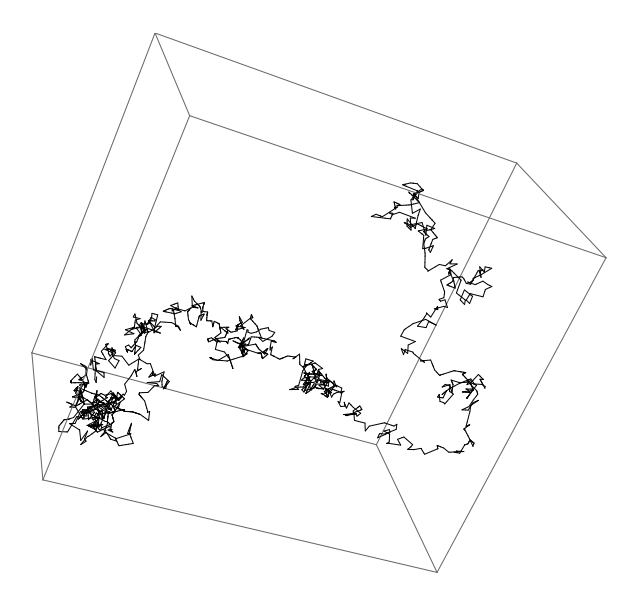


Figure 2.1: Simulation of a freely jointed chain, or a 3D random walk. Figure courtesy of [19].

2.1 Theory

2.1.1 Single Molecule Under Confinement

2.1.1.1 Polymer Physics Formalism

A polymer, such as DNA, is a large molecule composed of many repeating small subunits called monomers. A linear polymer (as opposed to branched or circular) is then essentially a string of monomers. Such a molecule can be represented as a 3D random walk where each step corresponds to the position of a monomer. The simplest model of a polymer is a random walk where the distribution of angles between the successive steps is uniformly random. This model is called the "freely jointed chain" [9] and can be visualized in Fig. 2.1.

This simplified picture already introduces two key concepts: contour length (L) and end-to-end length (R). The contour length is the length of the polymer from one end to the other, fully stretched out. In other words, the contour length is the number of steps/monomers (N) multiplied by step/monomer size (b). The end-to-end length on the other hand is the distance between the polymer ends in a particular polymer configuration (as opposed to fully stretched out). It is illustrated in Fig. 2.2. In the freely jointed chain model, the relationship between contour length, number of monomers, size of monomer, and end-to-end length is:

$$R = (bL)^{1/2} = bN^{1/2}. (2.1)$$

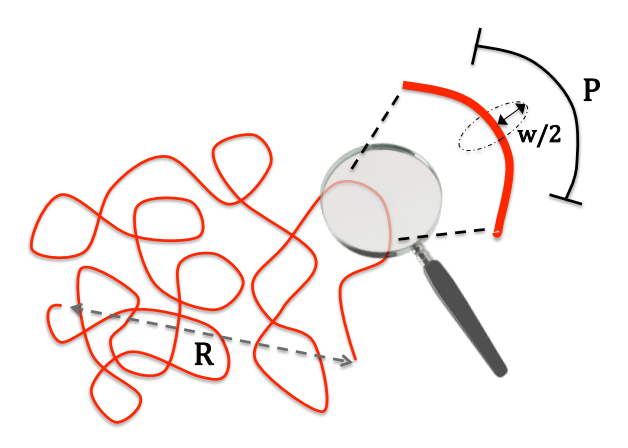


Figure 2.2: Illustration of end to end length, persistence length, and effective width. Figure courtesy of [19].

While some polymers (especially synthetic polymers) are very flexible and can really be described by a random walk with uniformly distributed angles, DNA is much more rigid: it is semi-flexible. Semiflexibility introduces one more key concept: persistence length (P). For a given position on the polymer, persistence length can be understood as the "distance in contour over which the DNA molecule 'forgets' its orientation" [26], as illustrated in Fig. 2.2. It is a measure of the rigidity of the polymer. In the case of DNA in a salt solution, persistence length depends on the sequence of DNA and on the ionic strength of the solution. The relationship between end-to-end length, contour length, and persistence length for a semiflexible polymer is [26]:

$$R^{2} = 2PL\left(1 + \frac{P}{L}\left[\exp\left(-\frac{P}{L}\right) - 1\right]\right). \tag{2.2}$$

In the $L\gg P$ limit (molecule is large), Eq. 2.2 reduces to $R^2\approx 2PL$, which corresponds to a random walk with step size of 2P, or a flexible molecule of monomer size 2P. In the $L\ll P$ limit (molecule is small), Eq. 2.2 reduces to $R^2\approx L^2$, which corresponds to a rigid rod of length L.

The previous models viewed the polymer as an ideal chain: two different monomers at different contour positions on the molecule can theoretically occupy the same physical space, meaning the chain can go through itself. In reality, this is of course impossible. A real chain exhibits self-avoidance: each segment of the polymer occupies a space excluded to other polymer segments. This concept is formalized as the 'excluded volume' (ν). We can understand the ideal chain as being infinitely thin, while the self-avoiding chain has a finite effective width (usually w but denoted d in the manuscript section; its value can depend on ionic strength). The excluded volume is therefore

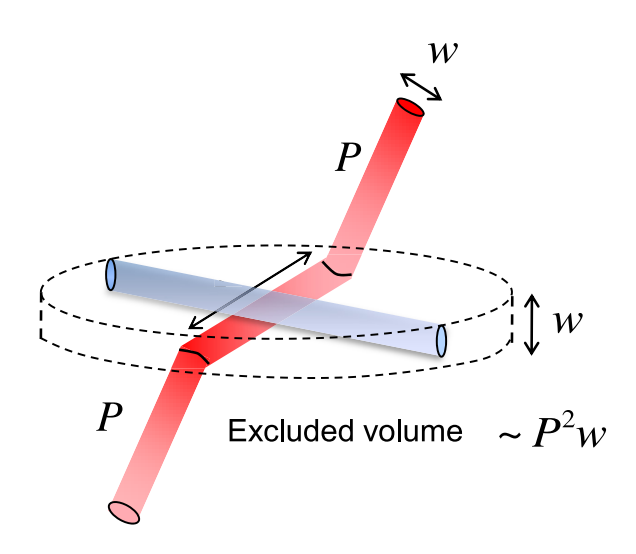


Figure 2.3: Illustration of excluded volume. Figure courtesy of [26].

a function of P and w, and a simple derivation gives $\nu \sim P^2 w$, as illustrated in Fig. 2.3. The excluded volume has the expected effect of swelling a self-avoiding polymer when compared with an ideal polymer of the same contour length. While for an ideal semiflexible chain, $R \sim 2PN^{1/2}$, for a real semiflexible chain [26],

$$R \sim 2PN^{3/5}$$
. (2.3)

The 3/5 exponent is called the Flory exponent.

The free energy of a self-avoiding polymer has two components. The first is an excluded volume component:

$$F_{\text{Ex.Vol.}} = \frac{1}{2} k_B T \nu \frac{N^2}{R^3},$$
 (2.4)

where k_BT is the thermal energy. This free energy decreases as R increases, and swells the polymer as expected. The second is an entropic component:

$$F_{\text{Entropy}} = \frac{3}{4PL}R^2. \tag{2.5}$$

This free energy increases as R increases, and shrinks the polymer. Entropy favours shrinking because there are more possible configurations for a shrunken polymer than for a more extended one. Adding the free energies together and minimizing with respect to R yields flory scaling for R.

For polymers under confinement, whether 1D, 2D or 3D, and also polymer solutions of a certain concentration, it is standard to use the 'blob' model. The idea is that a polymer's contour can be

^{1.} This is equivalent to $R \sim (2PL)^{1/2}$ given above since $L \sim 2PN$.

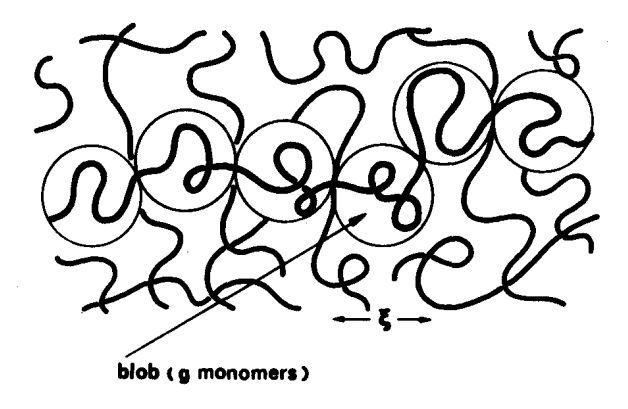


Figure 2.4: Illustration of polymers partitioning themselves into blobs. Figure courtesy of [11].

partitioned into one or more consecutive sections called blobs, as illustrated in Fig. 2.4. A blob is of a critical size such that a segment inside a blob only interacts with other segments within the blob; it does not interact with the outer environment or segments from other blobs. This critical size is a key concept that we will come back to later: it's called the correlation length (ξ).

2.1.1.2 Regimes of Confinement

Before we can start thinking about what happens to polymer solutions under confinement, it is helpful to think of the single molecule case. Sakaue worked through all possible confinement regimes for a single chain in strong confinement regime (SCR) [30]. While in weak confinement regime (WCR), the local volume fraction of the polymer inside a blob² is independent of polymer length, in SCR, the volume fraction does depend on polymer length. For the single molecule case, all 1D and 2D confinement fall into WCR while only 3D confinement can result in SCR. We shall see later than for systems with multiple molecules in solution, 1D and 2D confinement can also result in molecules being in SCR, when the concentration is high enough. Indeed, SCR is the right single molecule analogy to the polymer solution system we're studying.

Sakaue first explores the confinement regimes for flexible polymers [30]. In SCR, there are two possible scaling regimes: fluctuating semidilute (I) and semidilute in θ -solvent regime (II), as shown in Fig. 2.5. We can think of a flexible polymer this way: for high enough temperature (above θ , that is), in bulk the polymer is just a random walk of blobs, called thermal blobs, the size (ξ_{th}) of which is determined by the temperature and θ . Such a polymer, when put into a small cavity in SCR, will also partition itself into blobs of size ξ . Therefore, two things can happen: either $\xi > \xi_{th}$ because confinement is slightly less strong, or the opposite is true when confinement is stronger.

^{2.} Volume occupied by segments of the polymer inside the blob divided by total volume of blob, solvent included.

Theory Theory

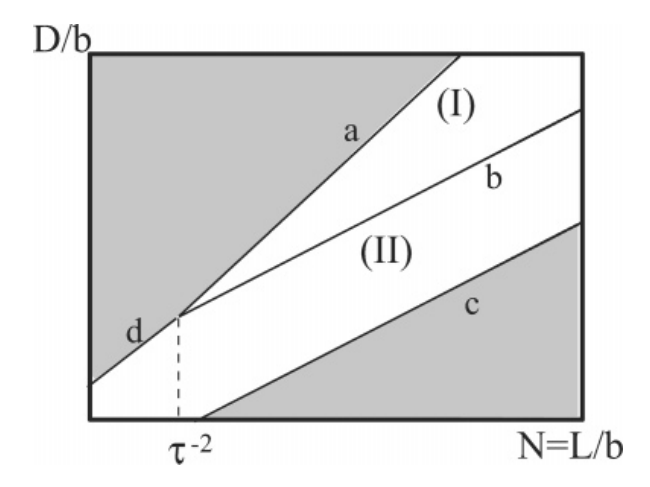


Figure 2.5: Confinement regimes for a single flexible chain: (I) fluctuating semidilute and (II) semidilute in θ -solvent regime. x-axis increases with chain length (or concentration) while y-axis increases with confinement size. Figure courtesy of [30].

The two scaling regimes correspond exactly to these two cases. Specifically, fluctuating semidilute regime is when $\xi > \xi_{th}$; the correlation length is larger than the thermal blob size, resulting in larger scale structures, or fluctuations than the thermal blobs, hence the name "fluctuating". Semidilute in θ -solvent regime is the opposite case.

Sakaue then moves on to the confinement regimes for semiflexible polymers [30], and the picture gets more complicated. There are five regimes in total: fluctuating semidilute (I), mean field semidilute (II), liquid crystalline (III), ideal chain (IV), and bending regime (V), as shown in Fig. 2.6. The first two are the semiflxible chain analogue to the two flexible chain regimes. The mean field theory, which applies in the mean field semidilute regime, is a way to simplify the model of interaction between chain segments. It models interactions by looking at one particular segment and its interaction with all other segments which is approximated as a field, thus reducing a many-body problem to a one-body problem. When confinement gets even stronger than in the mean field semidilute regime, correlation length decreases to the order of the persistence length, and we're in the liquid crystalline regime, where the segments behave like a liquid crystal which can be ordered or unordered.

There is another region where concentration is slightly lower than the mean field semidilute regime, and correlation length is larger than the confinement dimension. This is the ideal chain regime, called such because the entropy term of free energy is dominant compared to the excluded volume term. Mean field theory also applies in this regime. Finally, there is the bending regime, where confinement is very strong, and behaviour of the polymer depends strongly on the exact

Theory Theory

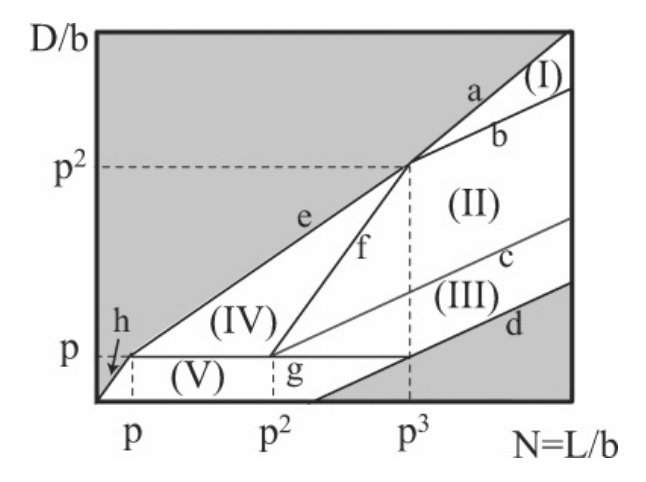


Figure 2.6: Confinement regimes for a single semiflexible chain: (I) fluctuating semidilute, (II) mean field semidilute, (III) liquid crystalline, (IV) ideal chain, (V) and bending regime. *x*-axis increases with chain length (or concentration) while *y*-axis increases with confinement size. Figure courtesy of [30].

flexibility of the polymer.

When trying to generalize the single molecule confinement regimes to solutions, we wonder if we will observe similar scalings as in the single molecule case. The critical question is, will mean field type scaling apply or would we observe fluctuating scalings instead?

2.1.1.3 Above the Overlap Concentration

We have seen above that single chains in SCR are well understood. (Single chains in WCR, so 1D or 2D confinement, are also well understood.) When we have many chains, but the solution is dilute enough such that the chains don't touch each other, these chains behave like single chains. But what happens when the solution is more concentrated and the chains do overlap? This threshold is aptly named the "overlap concentration"; below it, we're in dilute solution while above it, we're in semidilute solution.

An earlier paper by Daoud *et al.* explores solutions of flexible polymers in 1D and 2D confinement [6]. For 2D confinement, Daoud reports five regimes of confinement, as shown in Fig. 2.7. Regions A and B are not strongly affected by slit confinement while regions C, D and E are. Consequently, blobs in regions A and B are spherical while blobs in regions C, D and E are flatter, or pancake shaped. Regions A and C are dilute while regions B, D, and E are semidilute. The overlap

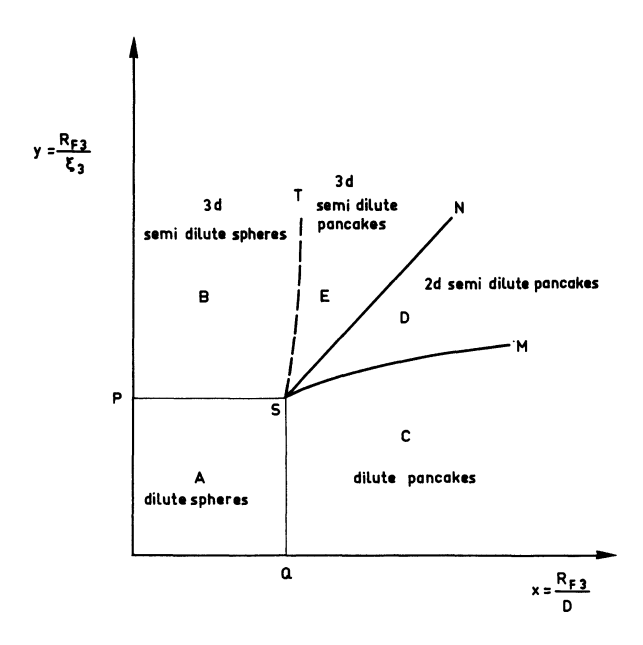


Figure 2.7: Confinement regimes for solution of flexible chains in slit-like (2D) confinement. x-axis decreases with confinement size while y-axis increases with concentration. Figure courtesy of [6].

concentration for less confined regions scales simply as

$$c_* \sim \frac{N}{R_F^3} \sim b^{-3} N^{-4/5}$$
 (2.6)

where R_F is the end to end length of one chain given by Eq. 2.3, also called the Flory radius. The overlap concentration for more confined regions scales as

$$c_* \sim \frac{N}{R_{\text{pancakes}}^2 D} \sim b^{-3} N^{-1/2} \left(\frac{b}{D}\right)^{1/2}$$
 (2.7)

where R_{pancakes} is the extent of a chain that has been flattened to a pancake shape in the slit, and D is the height of the slit.

Region A corresponds to dilute chains in very weak confinement, and so these chains behave like single chains in bulk. Region C corresponds to dilute chains in stronger confinement, and these chains behave like single chains in a slit. According to Sakaue's definition, this is still in WCR. Region B corresponds to semidilute solution in very weak confinement, so essentially in bulk also. What happens when we're above overlap concentration and confinement is high? Daoud predicts two cases: either the correlation length is smaller than slit dimension D (region E where solution

Theory Theory

behaves like in bulk), or it is larger (region D, a transition between regions C and E). This rings a bell! Region D is similar to the ideal chain regime (IV) of Sakaue's single semiflexible chain theory while region E is similar to the mean field semidilute regime (II).

So where does the system we're studying in this thesis fall within this framework? We have found that in our system, a mean field type theory works and the correlation length is larger than slit height. The closest analogue in Sakaue's system is region IV of single semiflexible chains, while the closest analogue in the theory of Daoud *et al.* is the transition region D. So we know for sure that there exists a regime for solutions of semiflexible polymers where the concentration is semidilute, mean field theory works, and the correlation length is large. Are there other possible regimes for solutions of semiflexible polymers? Of course, but they are beyond the scope of the present thesis.

2.1.2 Solution Under Confinement

2.1.2.1 Self-Consistent Field Approach

Now that the big picture of where our system is situated within the complex confinement regime space has been discussed, how do we go about theoretically modelling our particular problem? We used the mean field approach, also called the self-consistent field approach, following de Gennes [11]. The idea is this: we assume all monomers are identical and all interactions are repulsive and short-ranged. The interaction between two monomers i and j is defined as $\nu k_B T \delta(\mathbf{r}_{ij})$ where ν is the excluded volume and $\delta(\mathbf{r}_{ij})$ is a Kronecker delta function of the distance between the monomers. Then, instead of working with interactions between pairs (and triple, quadruple, etc.) of monomers, we look at one particular monomer and its interaction with all other monomers, which is approximated as a potential field (the mean field). The potential is therefore $U(\mathbf{r}) = \nu k_B T c(\mathbf{r})$ where $c(\mathbf{r})$ is the local concentration of monomers at position \mathbf{r} . Then we proceed as follows: we first assume an initial $U(\mathbf{r})$ from an initial $c(\mathbf{r})$ and use it to derive a new local concentration $c(\mathbf{r})$ consistent with $c(\mathbf{r})$ where $c(\mathbf{r}) \rightarrow c'(\mathbf{r}) \rightarrow c''(\mathbf{r}) \rightarrow c''(\mathbf{r})$ is used in the sequence $c(\mathbf{r}) \rightarrow c'(\mathbf{r}) \rightarrow c''(\mathbf{r}) \rightarrow c''(\mathbf{r})$. We then compute a new $c(\mathbf{r})$ from $c'(\mathbf{r})$ to derive $c''(\mathbf{r})$, and so on. Eventually, the sequence $c(\mathbf{r}) \rightarrow c'(\mathbf{r}) \rightarrow c''(\mathbf{r}) \rightarrow c''(\mathbf{r}) \rightarrow c''(\mathbf{r})$ is the local concentration of monomers at position $c'(\mathbf{r})$ and $c'(\mathbf{r})$ is the sequence $c'(\mathbf{r}) \rightarrow c''(\mathbf{r}) \rightarrow c''(\mathbf{r}) \rightarrow c''(\mathbf{r}) \rightarrow c''(\mathbf{r})$ will converge to a final $c'(\mathbf{r})$ that is consistent with $c'(\mathbf{r})$ is $c'(\mathbf{r})$ or with itself (the self-consistent field).

In practice however, we don't need to go through all the iterations to find the final concentration; we can use a Green's function instead. We set up the problem as such: a polymer chain is inscribed inside a lattice of step-size b, so instead of a random walk of step-size b with uniformly distributed angles between steps, only certain angles are permitted. A potential $U(\mathbf{r})$ acts on each monomer

Theory Theory

of the lattice-bound polymer. Therefore, the statistical weight of the whole polymer is

$$\exp\left(\frac{1}{k_B T}\left(U(\mathbf{r_1}) + U(\mathbf{r_2}) + \dots + U(\mathbf{r_N})\right)\right)$$
(2.8)

where $\mathbf{r}_1...\mathbf{r}_N$ are the position on the lattice of the monomers. We define the sum of this statistical weight over all possible paths of fixed ends $\mathbf{r}_1 = \mathbf{r}'$ and $\mathbf{r}_N = \mathbf{r}$ as

$$z^N G_N(\mathbf{r}', \mathbf{r}) \tag{2.9}$$

where z is the number of neighbours for one lattice site (e.g. 4 for a square lattice), and z^N is therefore the number of all possible different paths of N steps, and serves as a normalization factor. $G_N(\mathbf{r}', \mathbf{r})$ is the Green's function. We define the Green's function of 0 step as

$$G_0(\mathbf{r}', \mathbf{r}) = \delta_{\mathbf{r}', \mathbf{r}} \tag{2.10}$$

where $\delta_{\mathbf{r'},\mathbf{r}}$ is a Kronecker delta function. We can also write a Green's function of N+1 steps as a function of a Green's function of N steps, when both Green's functions share the same beginning and end positions:

$$G_{N+1}(\mathbf{r}',\mathbf{r}) = \frac{1}{z} \sum_{\mathbf{r}''} G_N(\mathbf{r}',\mathbf{r}'') e^{-\frac{U(\mathbf{r})}{k_B T}}$$
(2.11)

where the factor of 1/z is from our chosen normalization, $\sum_{\mathbf{r}''} G_N(\mathbf{r}', \mathbf{r}'')$ is the sum of all possible paths of N steps from position \mathbf{r}' to \mathbf{r}'' and \mathbf{r}'' is one step away from position \mathbf{r} , and $\exp(U(\mathbf{r})/k_BT)$ is the statistical weight of the last step. The relationship between the chains of N and N+1 steps are shown in Fig. 2.8. Using induction, we can recover

$$G_N(\mathbf{r_1}, \mathbf{r_N}) = \frac{1}{z^N} \sum_{\text{all paths}} \exp\left(\frac{1}{k_B T} \left(U(\mathbf{r_1}) + U(\mathbf{r_2}) + \dots + U(\mathbf{r_N})\right)\right)$$
(2.12)

which we had defined in the beginning.

Assuming that $\frac{U(\mathbf{r})}{k_BT}$ is small, we can Taylor expand Eq. 2.11 to become

$$G_{N+1}(\mathbf{r}',\mathbf{r}) = \frac{1}{z} \left(1 - \frac{U(\mathbf{r})}{k_B T} \right) \sum_{\mathbf{r}''} G_N(\mathbf{r}',\mathbf{r}'')$$
 (2.13)

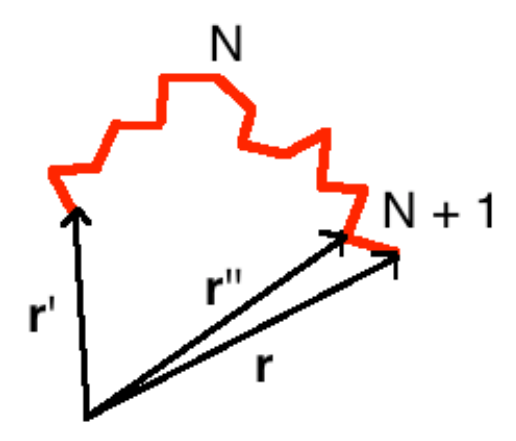


Figure 2.8: Illustration of the relationship between chains of N and N+1 steps as defined in Eq. 2.11.

Then assuming that $|\mathbf{r}'' - \mathbf{r}|$, or the step-size, is small, and Taylor expanding again,

$$\sum_{\mathbf{r}''} G_N(\mathbf{r}', \mathbf{r}'') = \sum_{\mathbf{r}''} (G_N(\mathbf{r}', \mathbf{r} - (\mathbf{r} - \mathbf{r}'')))$$

$$= \sum_{\mathbf{r}''} \left(G_N(\mathbf{r}', \mathbf{r}) + (\mathbf{r} - \mathbf{r}'') \frac{\partial G_N}{\partial \mathbf{r}} + \frac{1}{2} (\mathbf{r} - \mathbf{r}'')_{\alpha} (\mathbf{r} - \mathbf{r}'')_{\beta} \frac{\partial^2 G_N}{\partial \mathbf{r}_{\alpha} \partial \mathbf{r}_{\beta}} + \dots \right)$$
(2.14)

Rearranging terms of Eq. 2.13 and using the relation $\sum_{\mathbf{r}''} G_N(\mathbf{r}',\mathbf{r}'') = zG_N(\mathbf{r}',\mathbf{r}'')$, we get

$$G(\mathbf{r}',\mathbf{r})_{N+1} - G(\mathbf{r}',\mathbf{r})_{N} = \frac{U(\mathbf{r})}{k_{B}T}G(\mathbf{r}',\mathbf{r})_{N} + \frac{1}{z}\sum_{\mathbf{r}''}\left(1 - \frac{U(\mathbf{r})}{k_{B}T}\right)\left((\mathbf{r} - \mathbf{r}'')\frac{\partial G_{N}}{\partial \mathbf{r}}\right) + \frac{1}{2}(\mathbf{r} - \mathbf{r}'')_{\alpha}(\mathbf{r} - \mathbf{r}'')_{\beta}\frac{\partial^{2}G_{N}}{\partial \mathbf{r}_{\alpha}\partial \mathbf{r}_{\beta}} + \dots\right).$$
(2.15)

The term $\sum_{{f r}''} ({f r} - {f r}'') {\partial G_N \over \partial {f r}}$ vanish because

$$\sum_{\mathbf{r}''}(\mathbf{r} - \mathbf{r}'') = 0 \tag{2.16}$$

for a symmetric lattice. To figure out what happens to the term $\sum_{\mathbf{r}''} \frac{1}{2} (\mathbf{r} - \mathbf{r}'')_{\alpha} (\mathbf{r} - \mathbf{r}'')_{\beta} \frac{\partial^2 G_N}{\partial \mathbf{r}_{\alpha} \partial \mathbf{r}_{\beta}}$, let

Theory Theory

 $\mathbf{r} - \mathbf{r}'' = \widetilde{\mathbf{r}}$ and consider a cubic lattice

$$\sum_{\alpha=x,y,z} \sum_{\beta=x,y,z} \widetilde{\mathbf{r}_{\alpha}} \cdot \widetilde{\mathbf{r}_{\beta}} = \widetilde{\mathbf{r}_{x}} \widetilde{\mathbf{r}_{x}} + \widetilde{\mathbf{r}_{y}} \widetilde{\mathbf{r}_{y}} + \widetilde{\mathbf{r}_{z}} \widetilde{\mathbf{r}_{z}} + \widetilde{\mathbf{r}_{x}} \widetilde{\mathbf{r}_{y}} + \widetilde{\mathbf{r}_{y}} \widetilde{\mathbf{r}_{x}} + \widetilde{\mathbf{r}_{x}} \widetilde{\mathbf{r}_{z}} + \dots$$
 (2.17)

Since $\widetilde{\mathbf{r}_x}\widetilde{\mathbf{r}_x} + \widetilde{\mathbf{r}_y}\widetilde{\mathbf{r}_y} + \widetilde{\mathbf{r}_z}\widetilde{\mathbf{r}_z} = b^2$ and all mixed terms equal to 0, we can therefore say that

$$\widetilde{\mathbf{r}_{\alpha}} \cdot \widetilde{\mathbf{r}_{\beta}} = \delta_{\alpha\beta} \frac{b^2}{3} \tag{2.18}$$

and therefore

$$\frac{1}{z} \sum_{\mathbf{r}''} (\mathbf{r} - \mathbf{r}'')_{\alpha} (\mathbf{r} - \mathbf{r}'')_{\beta} = \delta_{\alpha\beta} \frac{b^2}{3}.$$
 (2.19)

Finally, the left-hand side of Eq. 2.15 can be written

$$G(\mathbf{r}',\mathbf{r})_{N+1} - G(\mathbf{r}',\mathbf{r})_{N} = \frac{G(\mathbf{r}',\mathbf{r})_{N+1} - G(\mathbf{r}',\mathbf{r})_{N}}{N+1-N} \approx \frac{\partial G_{N}}{\partial N}(\mathbf{r}',\mathbf{r}).$$
(2.20)

Considering Eq. 2.15 with Eq. 2.16, 2.19 and 2.20, we get

$$-\frac{\partial G}{\partial N} = -\frac{b^2}{6} \nabla^2 G + \frac{U(\mathbf{r})}{k_B T} G. \tag{2.21}$$

Eq. 2.21 has obvious resemblance with Schrödinger's equation:

$$-i \, \hbar \frac{\partial \psi}{\partial t} = -\frac{\hbar^2}{2m} \nabla^2 \psi + V(\mathbf{r}) \psi \tag{2.22}$$

where ψ is the wave function of the particle, $\hbar = \frac{h}{2\pi}$ is the reduced Plank constant, m is the particle mass, and $V(\mathbf{r})$ is a potential similar to $\frac{U(\mathbf{r})}{k_BT}$. We can therefore interpret Eq. 2.21 in term of Eq. 2.22: each chain conformation is equivalent to one path of a particle. The wave function corresponds to a superposition of amplitudes for different paths, and similarly, the Green's function, to a superposition of amplitudes for different chain conformations. In light of this similarity, we can solve the Green's function like we solve the Schrödinger's equation: by using an expansion in eigenfunctions. Consider the linear operator

$$\mathcal{G} = -\frac{b^2}{6}\nabla^2 + \frac{U(\mathbf{r})}{k_B T}.$$
 (2.23)

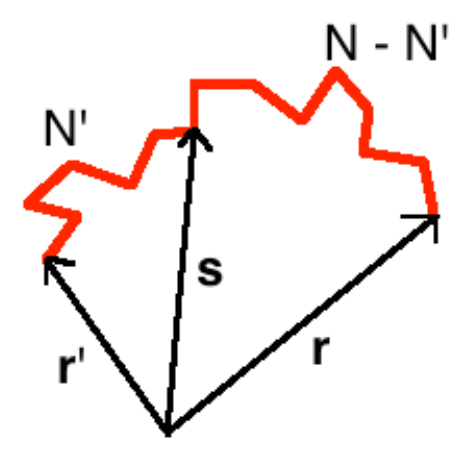


Figure 2.9: Illustration of two chains of N' and N-N' monomers joining at **s** to form a chain of N monomers.

We introduce a series of eigenfunctions $u_0(\mathbf{r}), u_1(\mathbf{r}), u_2(\mathbf{r}), ... u_k(\mathbf{r}), ...$ such that

$$\mathcal{G}u_k(\mathbf{r}) = \epsilon_k u_k(\mathbf{r}) \tag{2.24}$$

where ϵ_k is the eigenvalue of eigenfunction $u_k(\mathbf{r})$, and $\epsilon_0, \epsilon_1, \epsilon_2, ... \epsilon_k, ...$ is an increasing series with ϵ_0 being the minimum and corresponding to the ground state eigenvalue. We can show that these eigenfunctions $u_k(\mathbf{r})$ exhibit the properties of orthogonality and closure. Green's function can then be explicitly written in term of the eigenfunctions:

$$G_N(\mathbf{r}'.\mathbf{r}) = b^3 \sum_k u_k^*(\mathbf{r}') u_k(\mathbf{r}) e^{-N\epsilon_k}$$
(2.25)

where u_k^* is the complex conjugate of u_k . We can show that this form of the Green's function indeed satisfy Eq. 2.21. It also satisfies the property of Green's function:

$$G_N(\mathbf{r}', \mathbf{r}) = \sum_{\mathbf{s}} G_{N'}(\mathbf{r}', \mathbf{s}) G_{N-N'}(\mathbf{s}, \mathbf{r})$$
(2.26)

which basically means that a chain of N monomers which starts at \mathbf{r}' and ends at \mathbf{r} can be divided into two consecutive chains with arbitrary junction point \mathbf{s} , as shown in Fig. 2.9

Theory Theory

How does the Green's function relate to the familiar concept of concentration? We can define concentration $c(\mathbf{s})$ as the probability that at position \mathbf{s} , there is a monomer of a chain with arbitrary ends \mathbf{r}' and \mathbf{r} . We then introduce the statistical weight $\Phi(\mathbf{s})$ of a chain passing through \mathbf{s} regardless of end points \mathbf{r}' and \mathbf{r} and regardless of N. The statistical weight can be written in terms of the Green's function

$$\Phi(\mathbf{s}) = \frac{\sum_{\mathbf{r}'} \sum_{\mathbf{r}} \sum_{N'=0}^{N} G_{N'}(\mathbf{r}', \mathbf{s}) G_{N-N'}(\mathbf{s}, \mathbf{r})}{\sum_{\mathbf{r}'} \sum_{\mathbf{r}} G_{N}(\mathbf{r}', \mathbf{r})}$$
(2.27)

where the denominator is a normalization factor. And the statistical weight is related to concentration by

$$\Phi(\mathbf{s}) = b^3 c(\mathbf{s}). \tag{2.28}$$

Since the eigenfunction expansion of the Green's function has a factor of $e^{-N\epsilon_k}$, more weight is given to smaller values of ϵ_k , and so we expect the ground state to dominate. In the case of ground state dominance, let the ground state be written as $u_0(\mathbf{r}) = \psi(\mathbf{r})$ and the Green's function as $G_N(\mathbf{r}',\mathbf{r}) = b^3 \psi^*(\mathbf{r}') \psi(\mathbf{r}) e^{-N\epsilon_0}$. The statistical weight reduces to $\Phi(\mathbf{s}) = Nb^3 |\psi(\mathbf{s})|^2$ and therefore, $c(\mathbf{s}) = N|\psi(\mathbf{s})|^2$. As expected, if we integrate over the whole chain, we obtain $\int c(\mathbf{s}) d\mathbf{s} = N$. We can use ground state dominance and, as an exercise, apply it to the problem of an ideal chain confined between two repulsive walls at x=0 and x=D. Our potential is defined as U(x)=0 between the walls and $U(x)=\infty$ outside the walls. Therefore we have boundary conditions $\psi(0)=\psi(D)=0$ and equation

$$\mathcal{G}\psi(x) = -\frac{b^2}{6} \frac{d^2}{dx^2} \psi = \epsilon_0 \psi. \tag{2.29}$$

The solution is simple:

$$\psi = k \sin\left(\frac{\pi x}{D}\right),\tag{2.30}$$

where k is a constant. From

$$\mathcal{G}\psi(x) = -\frac{b^2}{6} \frac{d^2}{dx^2} \psi = \frac{b^2}{6} \left(\frac{\pi}{D}\right)^2 k \sin\left(\frac{\pi x}{D}\right) = \epsilon_0 \psi, \tag{2.31}$$

we find that $\epsilon_0 = \frac{1}{6} \left(\frac{\pi b}{D} \right)^2$. The concentration is therefore

$$c(x) = N|\psi(x)^2| = Nk^2 \sin^2\left(\frac{\pi x}{D}\right). \tag{2.32}$$

Now, let's use a potential that's self-consistent in the case of ground-state dominance. We can use a different normalization: $c(\mathbf{r}) = |\psi(\mathbf{r})|^2$, instead of $N|\psi(\mathbf{r})|^2$. The self-consistent potential is

then

$$U(\mathbf{r}) = k_B T \nu c(\mathbf{r}) = k_B T \nu |\psi(\mathbf{r})|^2. \tag{2.33}$$

Our Schrödinger's equation is now

$$\epsilon_0 \psi = -\frac{b^2}{6} \nabla^2 \psi + \nu |\psi|^2 \psi. \tag{2.34}$$

We can write the free energy of our chain conformation as

$$\frac{F}{k_B T} = \int \left(\frac{b^2}{6} |\nabla \psi|^2 + \frac{1}{2} \nu |\psi|^4 \right) d\mathbf{r}.$$
 (2.35)

We can get back Eq. 2.34 from Eq. 2.35 by taking the variational derivative of both sides with respect to ψ^* . On the left-hand side

$$\frac{\delta}{\delta\psi^*} \frac{F}{k_B T} = \frac{\delta}{\delta\psi^*} N\epsilon_0 = \frac{\delta}{\delta\psi^*} \int |\psi|^2 \epsilon_0 d\mathbf{r} = \int \frac{\delta}{\delta\psi^*} (\psi^*\psi) \epsilon_0 d\mathbf{r} = \int \epsilon_0 \psi d\mathbf{r}$$
(2.36)

The first term on the right-hand side is

$$\frac{\delta}{\delta\psi^*} \int \frac{b^2}{6} \nabla^2 \psi d\mathbf{r} = \int \frac{b^2}{6} \frac{\delta}{\delta\psi^*} \nabla \psi^* \cdot \nabla \psi$$

$$= \int \frac{b^2}{6} \left(\nabla \psi^* \cdot \frac{\delta}{\delta\psi^*} \nabla \psi + \nabla \psi \cdot \frac{\delta}{\delta\psi^*} \nabla \psi^* \right) d\mathbf{r}$$

$$= \int \frac{b^2}{6} \left(0 + \nabla \psi \cdot \frac{\delta}{\delta\psi^*} \nabla \psi^* \right) d\mathbf{r}$$

$$= \int \frac{b^2}{6} \nabla \psi \cdot \nabla \frac{\delta}{\delta\psi^*} \psi^* d\mathbf{r}$$

$$= \int_{S} \frac{b^2}{6} \frac{\delta}{\delta\psi^*} \psi^* \cdot \nabla \psi d\Gamma - \int \frac{b^2}{6} \nabla^2 \psi \cdot \frac{\delta}{\delta\psi^*} \psi^* d\mathbf{r}$$

$$= 0 + \int -\frac{b^2}{6} \nabla^2 \psi d\mathbf{r}$$
(2.37)

where on the 5th line, we use integration by parts. The second term on the right-hand side is

$$\frac{\delta}{\delta\psi^*} \int \frac{1}{2}\nu |\psi|^4 d\mathbf{r} = \int \frac{1}{2}\nu \frac{\delta}{\delta\psi^*} (\psi\psi^*\psi\psi^*) d\mathbf{r} = \int \frac{1}{2}\nu (\psi\psi\psi^* + \psi\psi^*\psi) d\mathbf{r} = \int \nu |\psi|^2 \psi d\mathbf{r} \quad (2.38)$$

Eq. 2.35 is the form of free energy we use in the manuscript section. It is a mean-field, self-consistent free energy.

2.1.2.2 Onsager Variational Principle

While the self-consistent field approach is powerful, it cannot be directly applied to our polymer solution problem, because of the interaction between the polymers and the compressive solvent flow. The presence of the solvent flow means the system is in steady-state, not equilibrium. This is where the Onsager variational principle comes in [8]. In a system of small particles and viscous liquid, the evolution of the system is determined by the balance of two forces: the force due to the potential driving the system to a minimum energy, and the frictional forces resisting this change. The Onsager variational principle allows us to find the evolution of such systems.

We start by writing the Langevin equation, which describes a particle undergoing Brownian motion, with an external field

$$-\xi \dot{x} - \frac{\partial U}{\partial x} + F_r(t) = m\ddot{x} = 0$$
 (2.39)

where the first term is the force due to friction, the second term is the force due to potential, and the third term is the random force. If the random forces are negligible, and we have a set of particles at positions $x = (x_1, x_2, ...x_N)$, then their time evolution can be written

$$-\sum_{j} \xi_{ij}(x)\dot{x}_{j} - \frac{\partial U(x)}{\partial x_{i}} = 0$$
 (2.40)

where ξ_{ij} are friction coefficients and U(x) is the potential energy of the system. Eq. 2.40 is a set of nonlinear differential equations. ξ_{ij} satisfy the Lorentz reciprocal relation, i.e. $\xi_{ij} = \xi_{ji}$. Also, $\sum_{ij} \xi_{ij}(x) \dot{x}_i \dot{x}_j \geq 0$ for all x_i and x_j . Therefore, ξ_{ij} is a positive definite matrix.

We define the Rayleighian [7]

$$R(\dot{x}, x) = \sum_{i} \frac{\partial U(x)}{\partial x_i} \dot{x}_i + \frac{1}{2} \sum_{ij} \xi_{ij}(x) \dot{x}_i \dot{x}_j.$$
 (2.41)

Since ξ_{ij} is positive definite, $R(\dot{x},x)$ has a unique minimum at the condition $\frac{\partial R}{\partial \dot{x}_i}=0$. In fact,

$$\frac{\partial R}{\partial \dot{x}_i} = \frac{\partial U}{\partial \dot{x}_i} + \frac{\partial}{\partial \dot{x}_i} \frac{1}{2} \sum_{ij} \xi_{ij}(x) \dot{x}_i \dot{x}_j \tag{2.42}$$

and the second term equals

$$\frac{\partial}{\partial \dot{x}_{i}} \frac{1}{2} \sum_{ij} \xi_{ij}(x) \dot{x}_{i} \dot{x}_{j} = \frac{\partial}{\partial \dot{x}_{i}} \frac{1}{2} \sum_{i} \xi_{ii}(x) \dot{x}_{i}^{2} + \frac{\partial}{\partial \dot{x}_{i}} \frac{1}{2} \sum_{i \neq j} \xi_{ij}(x) \dot{x}_{i} \dot{x}_{j} + \frac{\partial}{\partial \dot{x}_{i}} \frac{1}{2} \sum_{i \neq j} \xi_{ji}(x) \dot{x}_{j} \dot{x}_{i}$$

$$= \sum_{i} \xi_{ii}(x) \dot{x}_{i} + \frac{1}{2} \sum_{i \neq j} \xi_{ij}(x) \dot{x}_{j} + \frac{1}{2} \sum_{i \neq j} \xi_{ji}(x) \dot{x}_{j}$$

$$= \sum_{i} \xi_{ii}(x) \dot{x}_{i} + \sum_{i \neq j} \xi_{ij}(x) \dot{x}_{j}$$

$$= \sum_{i} \xi_{ij} \dot{x}_{j}.$$
(2.43)

Therefore

$$\frac{\partial R}{\partial \dot{x}_i} = \frac{\partial U}{\partial \dot{x}_i} + \sum_j \xi_{ij} \dot{x}_j = 0 \tag{2.44}$$

is equivalent to Eq. 2.40. The first term of the Rayleighian can be understood as the rate of change of potential energy when the particle i moves at velocity \dot{x}_i , while the second term is one half of the energy dissipated into heat due to friction per unit time. In other words, the Rayleighian describes how the free energy dissipates due to various processes, and its minimization is based on the principle of least energy dissipation [7].

We can derive the equations that govern particle sedimentation using the variational principle as an example. In this problem, the solute, or particles, has velocity \mathbf{v}_p , while the solvent has velocity \mathbf{v}_s . The average velocity of the solution is then

$$\mathbf{v} = \phi \mathbf{v}_p + (1 - \phi) \mathbf{v}_s \tag{2.45}$$

where ϕ is the volume fraction of the solute, or $\phi = b^3c$. There are two energy dissipation terms. The first is due to relative velocity between solvent and solute and has the form

$$\Phi_1 = \frac{1}{2} \int d\mathbf{r} \widetilde{\xi} (\mathbf{v}_p - \mathbf{v}_s)^2$$
 (2.46)

where $\widetilde{\xi}=\widetilde{\xi}(\phi)$ is a friction coefficient that depends on volume fraction (or concentration). Specifically, we expect $\widetilde{\xi}(0)=\widetilde{\xi}(1)=0$ while $\widetilde{\xi}_{\max}$ occurs at $\phi=1/2$. We can also write

$$\mathbf{v}_p - \mathbf{v} = \mathbf{v}_p - \phi \mathbf{v}_p - (1 - \phi) \mathbf{v}_s = (1 - \phi) (\mathbf{v}_p - \mathbf{v}_s)$$
 (2.47)

and therefore, Eq. 2.46 can be written

$$\Phi_1 = \frac{1}{2} \int d\mathbf{r} \xi (\mathbf{v}_p - \mathbf{v})^2 \tag{2.48}$$

where $\xi = \widetilde{\xi}/(1-\phi)^2$. $\xi \approx \widetilde{\xi}$ for small ϕ . The second contribution to energy dissipation is due to the spacial gradient of velocity:

$$\Phi_{2} = \frac{1}{4} \int d\mathbf{r} \eta \left(\frac{\partial v_{\beta}}{\partial r_{\alpha}} + \frac{\partial v_{\alpha}}{\partial r_{\beta}} \right)^{2}
= \frac{1}{4} \int d\mathbf{r} \eta \left[\nabla \mathbf{v} + (\nabla \mathbf{v})^{t} \right]^{2}.$$
(2.49)

Notice that the square really means tensor product. We have chosen to ignore the gradient between \mathbf{v}_p with itself, and \mathbf{v}_p with \mathbf{v} , which is fine for small volume fraction.

The free energy of the system is

$$A = \int d\mathbf{r} (f(\phi) - \rho \phi \mathbf{g} \cdot \mathbf{r})$$
 (2.50)

where $f(\phi)$ is the free energy due to mixing per volume, ρ is the difference in the density of solute and solution, and **g** is gravitational acceleration. We need $\partial A/\partial t$ to construct the Rayleighian, so

$$\dot{A} = \int d\mathbf{r} (f'(\phi)\dot{\phi} - \rho\dot{\phi}\mathbf{g} \cdot \mathbf{r}) = \int d\mathbf{r}\dot{\phi} (f'(\phi) - \rho\mathbf{g} \cdot \mathbf{r})$$
(2.51)

We can use the continuity equation $\dot{\phi} = -\nabla \cdot (\mathbf{v}_p \phi)$ and integrate by part:

$$\dot{A} = -\int d\mathbf{r} \nabla \cdot (\mathbf{v}_{p}\phi)(f'(\phi) - \rho \mathbf{g} \cdot \mathbf{r})$$

$$= -\mathbf{v}_{p}\phi(f'(\phi) - \rho \mathbf{g} \cdot \mathbf{r})\Big|_{-\infty}^{\infty} + \int d\mathbf{r}(\mathbf{v}_{p}\phi) \cdot (\nabla \cdot f'(\phi) - \nabla \rho \mathbf{g} \cdot \mathbf{r})$$

$$= 0 + \int d\mathbf{r} \mathbf{v}_{p} \cdot (\phi \nabla \cdot f'(\phi) - \phi \rho \mathbf{g})$$
(2.52)

Using the osmotic pressure $\Pi = \phi \frac{\partial f}{\partial \phi} - f$ and $\nabla \Pi = \frac{\partial f}{\partial \phi} \nabla \phi + \phi \nabla \frac{\partial f}{\partial \phi} - \frac{\partial f}{\partial \phi} \nabla \phi = \phi \nabla \frac{\partial f}{\partial \phi}$, we obtain

$$\dot{A} = \int d\mathbf{r} \mathbf{v}_p \cdot (\nabla \Pi - \phi \rho \mathbf{g}) \tag{2.53}$$

We need to add one Lagrange multiplier term to the Rayleighian to preserve the incompress-

Theory Theory

ibility criterion $\nabla \cdot \mathbf{v} = 0$. The Rayleighian is

$$R = \frac{1}{2} \int d\mathbf{r} \xi (\mathbf{v}_{p} - \mathbf{v})^{2} + \frac{1}{4} \int d\mathbf{r} \eta \left[\nabla \mathbf{v} + (\nabla \mathbf{v})^{t} \right]^{2} + \int d\mathbf{r} \mathbf{v}_{p} \cdot (\nabla \Pi - \phi \rho \mathbf{g}) - \int d\mathbf{r} p \nabla \cdot \mathbf{v}$$

$$= \frac{1}{2} \int d\mathbf{r} \xi (v_{p\alpha} - v_{\alpha})^{2} + \frac{1}{4} \int d\mathbf{r} \eta \left(\frac{\partial v_{\beta}}{\partial r_{\alpha}} + \frac{\partial v_{\alpha}}{\partial r_{\beta}} \right)^{2} + \int d\mathbf{r} v_{p\alpha} \left(\frac{\partial \Pi}{\partial r_{\alpha}} - \phi \rho g_{\alpha} \right) - \int d\mathbf{r} p \frac{\partial v_{\alpha}}{\partial r_{\alpha}}$$
(2.54)

Taking the variational derivative of R with respect to \mathbf{v} yields

$$\frac{\delta R}{\delta v_{\alpha}} = -\int d\mathbf{r} \xi (v_{p\alpha} - v_{\alpha}) - \int d\mathbf{r} \frac{\partial}{\partial r_{\alpha}} \eta \left(\frac{\partial v_{\beta}}{\partial r_{\alpha}} + \frac{\partial v_{\alpha}}{\partial r_{\beta}} \right) + \int d\mathbf{r} \frac{\partial p}{\partial r_{\alpha}} = 0$$
 (2.55)

using integration by part on the second and third terms. The resulting equation is therefore

$$\xi(\mathbf{v}_p - \mathbf{v}) + \nabla \cdot \eta \left[\nabla \mathbf{v} + (\nabla \mathbf{v})^t \right] = \nabla p \tag{2.56}$$

Taking the variational derivative with respect to \mathbf{v}_p yields

$$\frac{\delta R}{\delta v_{p\alpha}} = \int d\mathbf{r} \xi (v_{p\alpha} - v_{\alpha}) + \int d\mathbf{r} \left(\frac{\partial \Pi}{\partial r_{\alpha}} - \phi \rho g_{\alpha} \right) = 0$$
 (2.57)

The resulting equation is therefore

$$\xi(\mathbf{v}_p - \mathbf{v}) = -\nabla \Pi + \phi \rho \mathbf{g}. \tag{2.58}$$

This approach was used in the manuscript, with the only difference being that we used the mean-field self-consistent free energy from Section 2.1.2.1 instead.

2.1.2.3 Rescaling

After combining the approaches from the previous two sections, we find an equation governing the ground-state eigenfunction that has the same form as the Gross-Pitaevskii equation. The Gross-Pitaevskii equation describes the ground state of a quantum system of identical bosons, and is written [24]:

$$\left(-\frac{\hbar}{2m}\nabla^2 + V(\mathbf{r})\frac{4\pi\hbar^2 a}{m}|\psi(\mathbf{r})|^2\right)\psi(\mathbf{r}) = \mu\psi(\mathbf{r})$$
(2.59)

where $\mathbb{I}h$ is the reduced Plank constant, m is the mass of the particle, a is the scattering length, $V(\mathbf{r})$ is an external potential, and μ is the chemical potential. The 1D equation we derive for the ground-

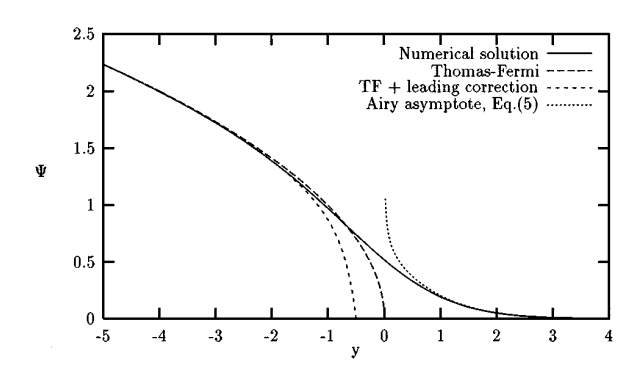


Figure 2.10: Numerical solution to Eq. 2.61 with approximations. The Thomas-Fermi curve corresponds to Eq. 2.62; the TF + leading correction curve corresponds to Eq. 2.65; the airy asymptote curve corresponds to Eq. 2.63. Figure courtesy of [24].

state eigenfunction (Eq. 3.18 in the manuscript section) corresponds exactly to a Gross-Pitaevskii equation where the external potential is a linear ramp:

$$\left(-\frac{\ln d^2}{2m}\frac{d^2}{dx^2} + Fx + \frac{4\pi \ln^2 a}{m}|\psi(x)|^2\right)\psi(x) = \mu\psi(x) \tag{2.60}$$

(F is a force acting on the particle).

Lundh et al [24] proposed a rescaling method to reduce Eq. 2.60 into the parameterless equation

$$\Psi'' = y\Psi + \Psi^3. \tag{2.61}$$

The rescaling is $y=x/\delta$ where $\delta=(\hbar/2mF)^{1/3}$ and $\Psi=\psi/b$ where $b=(2mF/\hbar)^{2/3}/8\pi a$. It is then possible to solve Eq. 2.61 numerically, or apply approximations. The Thomas-Fermi approximation ignores the second derivative and yields

$$\Psi = \sqrt{-y} \text{ for } y \le 0 \text{ and } \Psi = 0 \text{ for } y > 0. \tag{2.62}$$

For $y \ll -1$, this approximation is valid. We can also linearize Eq. 2.61 by ignoring the cubic term, and the solution is an Airy function, the asymptotic behaviour of which is

$$\Psi \approx \frac{k}{y^{1/4}} e^{-\frac{2}{3}y^{3/2}} \tag{2.63}$$

where k is a constant. This approximation only works for y>0. If we take the Thomas-Fermi solution as Ψ_0 and add a correction Ψ_1 to it such that the resulting solution is $\Psi=\Psi_0+\Psi_1$, we

find using perturbation theory that

$$\Psi_1 \approx \frac{1}{8y^2\sqrt{-y}} \tag{2.64}$$

and

$$\Psi \approx \sqrt{-y} \left(1 + \frac{1}{8y^3} \right). \tag{2.65}$$

The numerical solution to Eq. 2.61 as well as the approximations in Eq. 2.62, 2.63 and 2.65 are shown in Fig. 2.10. We have used a similar rescaling method in the manuscript, but used exact numerical solutions instead of the approximations. The numerical solution we computed for the rescaled equation perfectly matches the one provided by Lundh *et al* in Fig. 2.10.

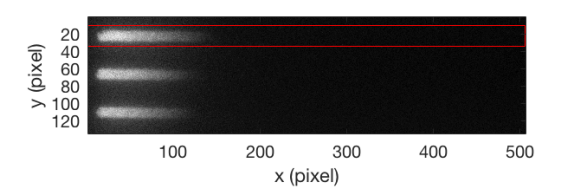


Figure 2.11: The first frame of the video taken with 79 ± 6 DNA, at flow speed of 1.13 μ m/s, with the region of interest shown in red rectangle.

2.2 Data Analysis Techniques

2.2.1 Obtaining Longitudinal Profiles

2.2.1.1 Image Processing Procedure

As the author of this thesis did not take the experimental data, we will not cover the data acquisition details. A summary of the experimental procedure can be found in the manuscript section. The important part for data analysis is what the raw data consist of: they are videos of an array of nanoslits containing a number of fluorescently dyed DNA molecules during steady-state compression. There are six sets of experiments that were retained in the manuscript: four sets were taken in 2 μ m wide slits and contained 79 ± 6 , 60 ± 6 , 57 ± 9 , and 50 ± 5 DNA molecules; two sets were taken in $10 \, \mu$ m wide slits and contained 154 ± 28 and 78 ± 19 DNA molecules. Each set of data contains five different steady-states videos corresponding to different solvent flows (ranging from $1 \, \mu$ m/s to $22 \, \mu$ m/s), and each video was imaged for 20-30 s at a frame rate of $100 \, \text{ms}$.

The image processing of the raw data is minimal. Using matlab, we read each video into a 3D array where the first two dimensions are the length and width of one image, and the third dimension is time. Since each video contains typically more than one slit, we manually draw a rectangle using the builtin function roipoly around the region of interest and only process the pixels inside the cropped region (the region of interested is shown by the red square in Fig. 2.11). Then for each video, we sum over the width of the slit, and take an average over all frames. The resulting 1D longitudinal time-averaged data vector is then normalized: it is divided by its total intensity I_{tot} and also by the pixel size Δx_{pix} . Normalizing the data individually for each data profile accounts for the effect of photobleaching over the time of the experiment. To find the number of molecules of each set of data, we divide I_{tot} by the total intensity of one molecule (which was imaged separately).

2.2.1.2 Background Subtraction

In the final version of the manuscript, we have decided not to subtract background noise at all. This is due to the special nature of how light scatters around our region of interest. As seen in Fig. 2.11, the light intensity of each packing seems to bleed around the packing into the dark regions around it, decaying with distance from the packing. If we plot each set of longitudinal data, we find that the intensity far from the packing decays exponentially on both sides of the packing (see Fig. 3.5(b) in the manuscript section). We therefore conclude that this tail is due to a wave-guiding effect of the packing intensity along the glass microfluidic device.

This effect poses a problem to the subtraction of background noise. If we use a region between slits to calculate our background intensity, this background region still contains some light intensity from the packings adjacent to it. The slits on our devices are too close to each other to provide a region free from wave-guiding light intensity between them. This means if we subtract this background intensity, we're altering the shape of our resulting data.

If we use the boundary of our region of interest to construct a background intensity, which we can do by using the matlab function roifill, we're also altering the shape of our resulting data. roifill uses Laplace's equation to fill in a region with a given boundary condition. We can interpret it as heat distribution: the boundary of the region has fixed temperature, while inside the region, heat is allowed to flow freely. The solution obtained from solving Laplace's equation is the final steady-state temperature profile inside the region for the given boundary conditions. This algorithm works well for background subtraction if the boundary of our region of interest really only exhibit background intensity, but it is not the case in our data. In fact, we had processed our data this way in the past, and it did alter the tail of our profiles, as shown in Fig. 2.12. This is why we stopped using this method.

2.2.2 Generating Numerical Solutions using FlexPDE

2.2.2.1 Using Adiabatic Expansion

In order to compare the experimental data with the theory, we need to compute the numerical solutions to the PDE predicted by the theoretical model (the LRCPDE, Eq. 3.18, in the manuscript section). Solving this PDE is not trivial due to the third order term. We used the commercial PDE solver FlexPDE to compute our numerical solutions, and it cannot solve nonlinear eigenvalue problems. Without the third order term, the solutions are simple: they are the Airy functions (Ai(x) and Bi(x)). One method is inspired from quantum mechanics: we start with the linear solution, then use adiabatic expansion to slowly introduce the third order term.

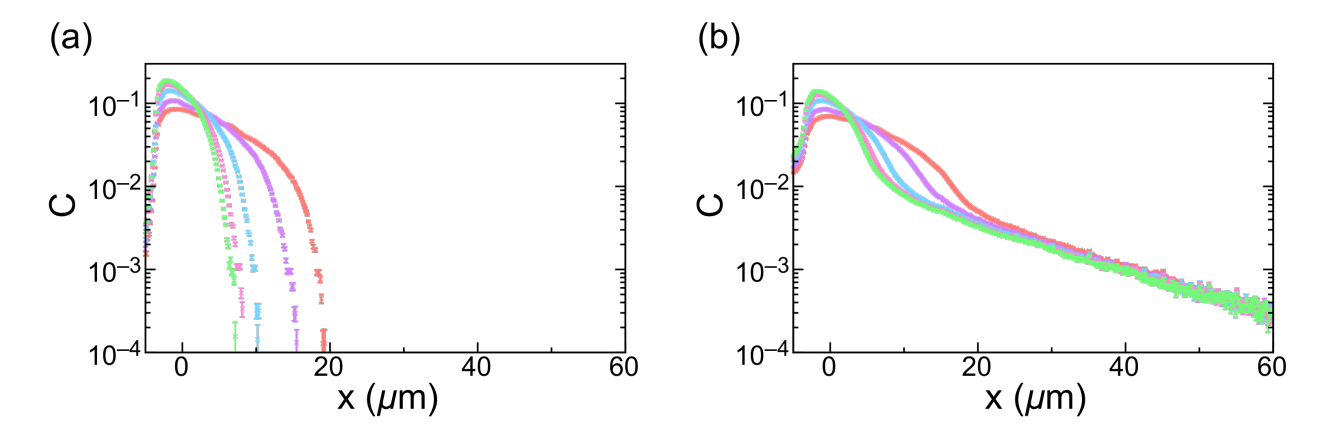


Figure 2.12: (a) Concentration profiles for 79 ± 6 DNA, with roifill background subtraction. The pale-red curve corresponds to a pressure of 27 mbar, purple curve 47 mbar, blue-curve 96 mbar, pink curve 151 mbar and green curve 196 mbar. (b) Concentration profiles for the same dataset, without any background subtraction. Note the difference in the tails. The tails in (a) quickly drop to 0.

We start by computing the numerical solutions to the linear equation without the third order term, which we call u_0 . We define our region as bounded by positions x=0 and x=L and our boundary condition is that $u_0=0$ at x=0 (the barrier end of the slit). When the parameter m=1, the solution corresponds exactly to $\operatorname{Ai}(x)$, while when $m\neq 1$, the solutions are rescaled by m ($\operatorname{Ai}(mx)$). The initial solutions are normalized such that $\int_0^L dx |u_0|^2 = 1$. This initial function u_0 is fully real, but when we solve the nonlinear Schrödinger's equation using adiabatic expansion, we use a complex function $u=u_r+u_i$ where u_r is the real part and u_i is the imaginary part ($|u|^2=u_r^2+u_i^2$ as expected). The boundary condition then becomes $u_r=0$ and $u_r=0$ at x=0. We introduce the nonlinear term gradually, converging to the desired value exponentially. The time-dependent Schrödinger's equation which we solve interatively is

$$i\frac{\partial u}{\partial t} = -m\frac{\partial^2 u}{\partial x} + \left(1 - e^{\frac{t}{t_r}}\right)(u_r^2 + u_i^2)u + vxu \tag{2.66}$$

where t_r is the timescale of the convergence of the nonlinear term. The time-step used to solve the Schrödinger's equation is several order of magnitudes smaller than t_r while the the computation ends when t reaches $t_{\rm end}=10t_r$. Making the time-step and t_r larger makes the situation less adiabatic (the norm of u drops more at each time-step); making $t_{\rm end}$ small gives less time for the system to converge. But using small time-step and t_r as well large $t_{\rm end}$ increases the physical computation time (computing the entire set of solutions necessary for curve fitting can take upwards of 12 hours).

For each time-step, we monitor the value of $|u|^2=u_r^2+u_i^2$ at each point between x=0 and x=L, as well as the value of $\epsilon^2=\int_0^L dx |-m\frac{\partial^2 u}{\partial x}+(1-e^{t/t_r})(u_r^2+u_i^2)u+vxu|^2$, which corresponds to the square of the energy of u at the given time-step. If the process was completely adiabatic, the final values of u(x) correspond to the ground-state solution, while ϵ is the ground-state eigenvalue. However, because of the discreteness of our time-step and computation, our process is not entirely adiabatic, and so the final u(x) is a mixture of the ground state and the first few excited states. We know this because the values of $|u|^2$ and ϵ^2 oscillate with time while converging exponentially. We therefore need to explicitly compute the eigenstates and eigenvalues from the values of $|u|^2$ and ϵ^2 .

We compute the eigenstates/eigenvalues with a matlab code which reads the time evolution of $|u(x)|^2$ and ϵ^2 . We also assume that only the ground state ψ_0 and the first excited state ψ_1 are present (which is not entirely true, but is good enough for our purposes). So

$$u = a_0 \psi_0 e^{iE_0 t} + a_1 \psi_1 e^{iE_1 t} \tag{2.67}$$

where a_0 and a_1 are constants that would have been the probability amplitude of each eigenstates, had the norm of u been exactly 1. Therefore

$$|u(x)|^2 = a_0^2 |\psi_0(x)|^2 + a_1^2 |\psi_1(x)|^2 + 2a_0 a_1 \psi_0(x) \psi_1(x) \cos((E_1 - E_0)t)$$
(2.68)

and

$$\epsilon^2 = a_0^2 E_0^2 + a_1^2 E_1^2 + 2a_0 a_1 E_1 E_2 \left(\int_0^L \psi_0(x) \psi_1(x) dx \right) \cos((E_1 - E_0)t). \tag{2.69}$$

We take the last few oscillations towards the end of the time evolution of $|u|^2$ and ϵ^2 and remove the remaining slope due to the exponential convergence (by fitting the time evolution to a linear function and subtracting the slope while maintaining the mean value of the time evolution). We then perform a Fourier transform of the oscillations. We obtain the frequencies and amplitudes of the oscillations. The first peak in freaquency corresponds to the difference in energy of the ground and the first excited states. The first peak frequency of $|u|^2$ and ϵ^2 are the same and equal $f = |E_1 - E_0|/2\pi$. The amplitude of the peak frequency of $|u(x)|^2$ corresponds to $A_u(x) = 2a_0a_1\psi_0(x)\psi_1(x)$. The time-averaged value of the last few oscillations of $|u(x)|^2$ is $M_u = a_0^2|\psi_0(x)|^2 + a_1^2|\psi_1(x)|^2$ while the time-averaged value ϵ^2 is $M_\epsilon = a_0^2E_0^2 + a_1^2E_1^2$. We obtain

$$a_0^2 |\psi_0(x)|^2 = \frac{1}{2} \left(M_u + \sqrt{M_u^2 - A_u^2} \right)$$

$$a_1^2 |\psi_1(x)|^2 = \frac{1}{2} \left(M_u - \sqrt{M_u^2 - A_u^2} \right).$$
(2.70)

Therefore $|\psi_0(x)|^2$ is just $a_0^2|\psi_0(x)|^2$ normalized, and similarly for $|\psi_1(x)|^2$. We find the probability p_0 of ψ_0 by dividing the norm of $a_0^2|\psi_0(x)|^2$ by the norm of $|u|^2$ and the probability p_1 of ψ_1 by dividing the norm of $a_1^2|\psi_1(x)|^2$ by the norm of $|u|^2$. As expected, $p_0 + p_1 = 1$. Finally, we find

$$E_0 = 2\pi f p_1 + \sqrt{M_{\epsilon} - (2\pi f)^2 p_0 p_1}$$

$$E_1 = 2\pi f p_0 + \sqrt{M_{\epsilon} - (2\pi f)^2 p_0 p_1}.$$
(2.71)

We can then use $|\psi_0(x)|^2$ and E_0 for our fitting purposes.

Since we need to calculate the numerical solutions for a whole grid of values of m and ξ^2 in order to be able to fit our data to the numerical solutions, computation time is very long. Also, the process is not entirely adiabatic, and our approximation that u is only composed of the ground state and the first excited state is not entirely accurate. As a result, the profiles for $|\psi_0(x)|^2$ that we obtain are not entirely right. In particular, we observe still some oscillations in the tails of these profiles, especially when plotted in log-linear (see Fig. 2.13(a)). It is crucial that the tails of the numerical solutions be accurate since the most striking feature of the model that we're fitting to are the tails. With the level of error that we have using the adiabatic method, the fitting did not work very well. We ultimately used another method to compute numerical solutions.

2.2.2.2 Using Non-Adiabatic Time Evolution Equation

Since FlexPDE could not solve nonlinear eigenvalue problems directly, the adiabatic method is the only one that allows us to find the eigenvalue in our nonlinear PDE. But not being able to find the eigenvalue is not an issue if we don't need the eigenvalue in the first place. In our problem, the eigenvalue corresponds to a translation of the whole profile along the x-axis. This translation is crucial to the profile only if we set the boundary condition u=0 at x=0. If we set no boundary condition, the profile looks like an infinite ramp at x < E, and the tail region starts at x=E, with values at x>E decaying asymptotically to 0. Where we place E doesn't matter, so we can set E=0. Since we decided to fit only the ramp and tail portions of our experimental profiles (because the boundary portion depends on the exact geometry of our slit barrier, which is unknown), we are free to set E=0 and instead introduce the translation of the profile x_0 as a fitting parameter which doesn't depend on the model.

As we don't need the eigenvalue anymore, we can solve our PDE using a simple time-dependent method. We set our region from x = -L to x = L, with no boundary conditions for ψ , and the

equation that we solve iteratively is

$$\xi^2 \frac{\partial \psi}{\partial x} - \psi^3 - mx\psi = \frac{\partial \psi}{\partial t}$$
 (2.72)

where the right-hand side is an artificially introduced time dependence of ψ that decays to 0 for large time t. ψ is the ground-state exactly (not a composite state), and is fully real. The initial value of $\psi(x)$ can be set to a large constant. When we plug it in Eq. 2.72, the first term on the left side is 0 since $\psi(x)$ is a constant, while the next two terms have large negative values, and therefore $\frac{\partial \psi}{\partial t} \ll 0$. Hence the value of $\psi(x)$ lowers gradually, until $\frac{\partial \psi}{\partial t}$ converges to 0. The final value of $\psi(x)$ is the ground-state and only needs to be squared $(|\psi(x)|^2 = c(x))$ before we can perform a fitting.

This method, due to the simplicity of its variables and equations, is at least an order of magnitude faster than the adiabatic method. Using a larger grid of values of m and ξ^2 , all numerical solutions can be computed in a matter of minutes. We don't need a complicated program to extract the ground-state from the raw solutions, and the accuracy in the tail is much improved. A comparison for solutions obtained using the adiabatic and non-adiabatic methods is plotted in Fig. 2.13 (solutions have been rescaled according to Eq. 3.22 and 3.23 in the manuscript section for comparison purposes). The non-adiabatic method, with its higher quality solutions, is used in the final manuscript.

2.2.3 Fitting Data to Theory

2.2.3.1 Fitting Procedure

In order to fit the model to our data, we used a few matlab codes. The first code creates the numerical solutions by specifying a grid of values of parameters and running FlexPDE to compute the solutions for these values. Instead of directly using m and ξ^2 as the varied parameters, we used ξ^2 and $v=m/\xi^2$ because these two parameters are independent of each other. We used 19 values of ξ^2 ranging from 1/3 to 1/50, with values more closely spaced for smaller ξ^2 because the profiles vary faster between values of ξ^2 for smaller ξ^2 . We used 17 values of v ranging from v0.03 to 1.5, with values more closely spaced for smaller v1 for the same reason. For each set of parameters, the numerical solution is computed at v2 equally spaced points on the v3-axis between v3-axis between v4-axis between v5-axis between v6-axis between v

The second code reads the numerical solutions obtained by FlexPDE from the first code, and

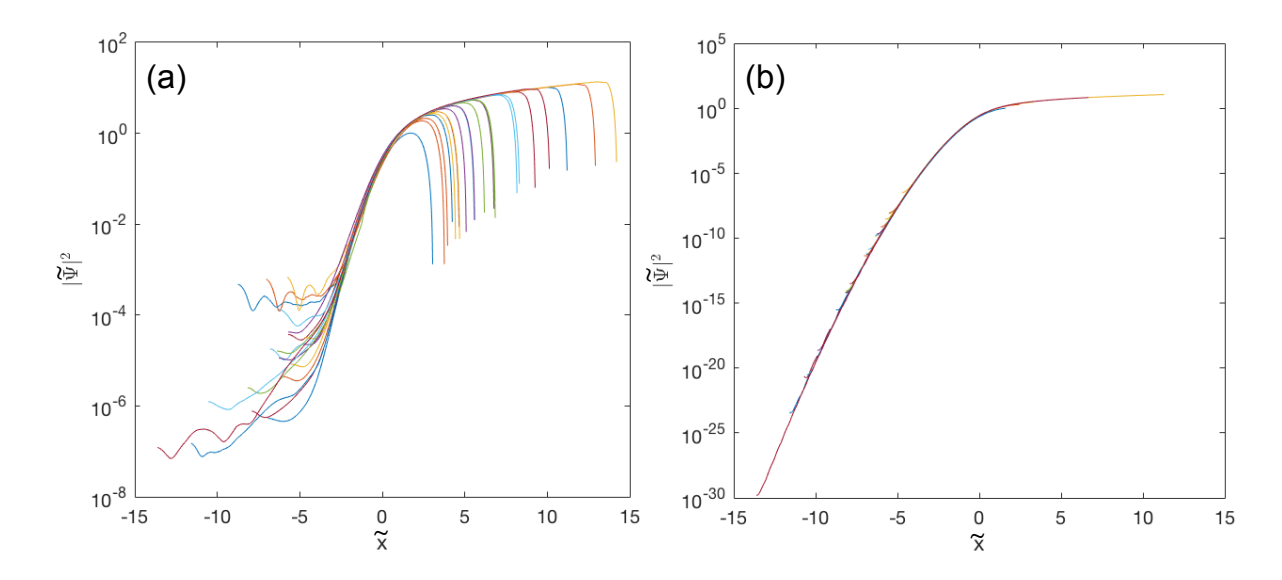


Figure 2.13: (a) Rescaled numerical solutions obtained using the adiabatic method. The tail region $(\widetilde{x} < 0)$ exhibit oscillations and don't collapse. (b) Rescaled numerical solutions obtained using the non-adiabatic method. The tail region $(\widetilde{x} < 0)$ collapse almost perfectly. Note that the adiabatic solutions include the boundary region $(\widetilde{x} \gg 0)$, the portion of the curves that don't collapse) while the non-adiabatic solutions don't.

creates an interpolation matrix of solutions that can be used for data fitting. It uses the built-in function scatteredInterpolant, which can interpolate between points that are scattered rather than equally spaced. scatteredInterpolant builds an interpolation matrix from the grid of numerical solutions, and the resulting matrix is evenly and finely spaced between parameters. This matrix has the interpolated values of $|\psi|^2$ for each of the 100 different values of ξ^2 , 100 different values of v and 000 values of v (the range of each parameters is bound by the range of the numerical solutions).

The third code fits the experimental data to the interpolation matrix. It uses the built-in function lsqcurvefit and fits the data to the interpolated values of the theoretical $|\psi|^2$ which has been convolved with the Line Spread Function (see next section). Each set of data (consisting of five profiles with different flow speed but the same number of molecules) is fitted together. The fitting parameters are: five values of slope m (different for each profile), five values of x_0 which is the x-axis translation of the curve (also different for each profile), one value of ξ^2 (the same for all five profiles), and two values that determine the LSF (the same for all five profiles).

2.2.3.2 Line Spread Function

The LSF is an effect that our experimental setup has on our observations. It has two components: the first arises from the microscopy instruments, while the second arises from the wave-guiding effect of our devices. The first component has the effect of spreading the intensity of sharp features of the sample. Any two dimensional image obtained using any microscope is equivalent to the convolution of the actual light intensity of the imaged sample with an Airy function (which can sometimes be approximated as a Gaussian). In 1D, the corresponding form of this component of the LSF is a Struve function (exact form given by Eq. 3.26 in manuscripte). The width of the Airy function (upon which depends the width of the Struve function) is determined experimentally by imaging a fluorescent bead and fitting the intensity with the convolution of a sharp 2D circle and an Airy function. The width is extracted from the fit.

The second component of the LSF is specific to our device and has the form of an exponential as discussed earlier in Section 2.2.1.2 (exact form given by Eq. 3.27). The ratio of the strength of the first and the second components of LSF (A), as well as the decay length of the exponential (a), are both fitting parameters when fitting each set of data to the model.

Because of the effect of the LSF has on our data, we have to convolve the theoretical model with the LSF while fitting it to our data. But once the LSF is obtained from the fitting, can we deconvolve the data from the LSF, and then fit it to the unconvolved theoretical model? We have tried to do that following the method given in [33]. We used a least square deconvolution method with diagonal loading to reduce the effect of noise. We compute the convolution matrix H using function convmtx from the LSF and the x values of the data. Then the deconvolved data is given by

$$C_{\text{deconv}} = (H' \cdot H + \lambda I(N)) \setminus (H' \cdot C_{\text{conv}}); \tag{2.73}$$

where H' is the transpose matrix of H, λ is the diagonal loading strength and can be varied to get better results, I(N) is an identity matrix of size N x N, and "\" is right-matrix division. This deconvolution works, but due to the noise in the data, there are a lot of oscillations in the deconvolved profiles. We then tried to Fourier transform the deconvolved profiles, set all frequencies above above a threashold to zero, then inverse Fourier transform the profiles. This does remove most of the oscillations, but some oscillations are still visible, especially when plotted in log-linear. We would expect the perfectly deconvolved data to rescale perfectly to the solution of the parameterless Schrödinger's equation (Eq. 3.24 in manuscript), but due to the oscillations, this is not observed. The deconvolved, frequencies-removed profiles are plotted in Fig. 2.14(a) while the rescaled versions are plotted with the solution to the parameterless equation in Fig. 2.14(b). Be-

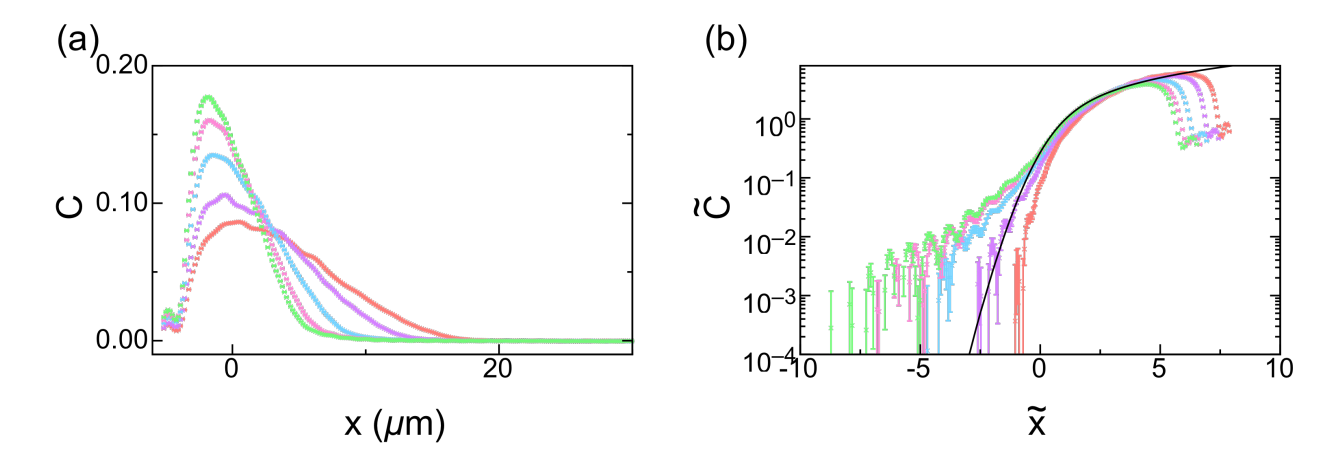


Figure 2.14: (a) Concentration profiles for 79 ± 6 DNA, after deconvolution and frequencies removing. The pale-red curve corresponds to a pressure of 27 mbar, purple curve 47 mbar, blue-curve 96 mbar, pink curve 151 mbar and green curve 196 mbar. (b) The same profiles, now rescaled, with the black line being the numerical solution to the parameterless equation. Curves are expected to collapse with the black line, but this is not observed due to the oscillations in the tails.

cause deconvolution yields inconclusive results, it has not been included in the manuscript.

Chapter 3

Compression of Nanoslit Confined Polymer Solutions

3.1 Preface to the Manuscript

In the previous chapter, we have covered a theoretical background for the content in the manuscript. We have seen how single semiflexible polymers behave in confinement, and how we can try to extend the picture to semidilute solutions of semiflexible polymers. We have covered the self-consistent field approach and the Onsager variational approach, both of which form the basis of the theory presented in the manuscript. We have discussed in detail the data analysis approaches used in the manuscript. The present chapter presents the manuscript, tying the loose ends introduced in the previous chapter. It presents the concept of our experiment, the experimental procedures, the theory we developed to model the experimental data, and an in depth analysis and discussion of our data and how it compares with the theoretical model. The last section of this chapter covers details of the theoretical derivation omitted in the published manuscript.

3.2 Abstract

Many systems of biophysical and technological interest consist of multiple interpenetrating chains in a confined volume, i.e., a confined polymer solution. Using nanofluidic approaches developed originally for the study of single chains in confined geometries, we develop an assay to create confined polymer solutions on-chip, and then probe the solution response to applied compressive forcing. In our approach, multiple chains are introduced into a nanoslit via hydrodynamic flow, and are then concentrated against a barrier that is permeable only to solvent. For sufficiently high concentration, the compressed solution profile can be described by a mean-field polymer model based on Doi's two-fluid approach, with the chain free energy described by a Ginzburg type free energy functional. This theory furnishes a partial differential equation based description of the concentration profile in terms of a nonlinear Schrödinger type equation, providing a general theoretical framework for modelling confined polymer solution dynamics.

3.3 Introduction

The development of nanoanalytical devices for single-molecule DNA sensing and manipulation has led to extensive research on how confinement alters the conformation of single polymer chains. In particular, polymer equilibrium conformation can be 'sculpted' via control of the enveloping confinement geometry and degree of imposed confinement [26]. Nanochannels extend individual polymer molecules for high throughput mapping [29, 23, 28]. Nanocavity structures can capture

37 Introduction

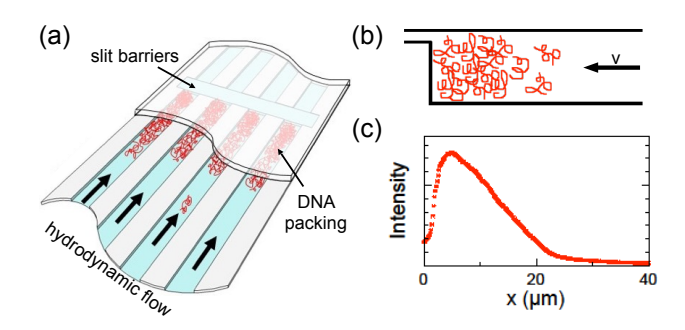


Figure 3.1: (a) Schematic showing dense packing of DNA against a slit-barrier inside an array of nanoslits. (b) Cross section of a slit along the channel axis, with the slit barrier on the left side. (c) One-dimensional fluorescence intensity profile along the channel axis extracted for a typical packing as shown in (b). This packing had 79 ± 6 DNA molecules, and an applied pressure of 27 mbar (corresponding to a flow speed of $1.13 \,\mu\text{m/s}$).

and store individual chains [27, 21, 20]. These applications have motivated extensive experimental, simulation-oriented and theoretical efforts to map out scaling regimes of confined chains in nanochannel [26, 36, 4], nanoslit [5] and cavity [16, 31, 30] geometries.

Yet, while the equilibrium properties of *single*-chains in simple geometries are now well-understood, we have a relatively poor understanding of confined *multiple* chain systems, i.e., *confined polymer solutions*. From an application perspective, understanding confined polymer solution behaviour is as important as understanding confined single chains. For example, there is a need to understand rheological properties of concentrated polymer solutions in nano/micron sized conduits for characterizing a range of micro/nanofluidic technologies using complex fluids [12]. Even in the context of nanofluidic devices designed for single-molecule manipulation, concentrated "plugs" of chains can build up in regions where there is a sharp change in confinement due to entropic trapping [13], e.g., at a microchannel/nanochannel junction or pore entrance. These concentrated polymer plugs may influence the rate at which molecules traverse the barrier and, hence, the tendency of devices, to "clog". Future nanofluidic device designs, integrating a range of features of varying size scale such as pores inside nanochannels [38], may be particularly susceptible to formation of such local "solution" regions. Lastly, quantifying confined polymer solutions is a first step towards understanding complex multiple chain systems in a biological context, such as chromosomal organization in the nucleus [2].

While knowledge of single chain behaviour is sufficient to quantify confined dilute solutions, new behaviours emerge as the chain concentration increases and the confined coils interpenetrate so that the system enters a "confined semi-dilute solution regime" [11]. Confined semi-dilute so-

38 Introduction

lutions of flexible chains were first described by de Gennes at the scaling level [6]. This theory has been tested in simulations [35] and experiments in porous media [22] but not yet in experiments conducted in nanofluidic systems with rigorously defined geometries. Moreover, DNA is semiflexible, with a persistence length P around 50 nm in typical buffer conditions [26]. Semiflexible chains can have special scaling regimes in confinement and in bulk where mean-field descriptions are exact and the classical de Gennes theory for flexible chains is no longer correct (in flexible chain theory, concentration fluctuations have a non-negligible effect on scaling exponents) [16, 31]. These special mean-field scaling regimes are termed "marginal solution regimes" in classical solution theory [1, 32]; in the special case of nanochannel and nanoslit confinement they are called "extended de Gennes regimes" [36, 26]. The question of whether a confined semiflexible chain will adopt mean-field or flexible scalings is highly non-trivial; complex scaling phase spaces exist as a function of chain size and confinement scale that determine the appropriate description [30]. In our studies involving compressing single DNA molecules with a sliding-piston assay, we have also observed that mean-field behaviour holds [17, 18]. An interesting question is whether mean-field scaling also applies to systems with multiple DNA chains in confinement. Finally, even for singlechains, we are just beginning to develop approaches for quantifying non-equilibrium behaviour in confinement [17, 18]. We expect local solutions in nanofluidic devices to be highly dynamic, due to continuous chain transport, chain escape and relaxation of concentrated regions. As in the case of single chains, we need approaches to extend equilibrium models to non-equilibrium scenarios [18], but it is even more critical in the multi-chain case, due to the difficulties of extending computationally intensive Brownian dynamic approaches [14] to many-polymer systems.

Here we develop a nanofluidic assay for creating concentrated polymer solutions in a nanoslit, analogous to devices used for single-chain manipulation. In this approach, an array of nanoslits is terminated at one end via a slit-barrier, thus permitting fluid flow, but blocking the passage of single coils. Multiple coils are introduced into the slits and then pack at the slit barrier (Fig. 3.1(a)), leading to controlled formation of a polymer solution. The degree of chain concentration can be tuned by varying the external hydrodynamic flow, which is induced by an applied positive pneumatic pressure. The integrated chain packing concentration along the channel axis (Fig. 3.1(b-c)), a function of position from the slit-barrier, encodes key information regarding solution behaviour, and is the fundamental observable. We find that the concentration profile, when the packing concentration is high enough, can be described by a "universal" mean-field theory based on M. Doi's two-fluid model [10] and the Onsager variational principle [8]. A partial differential equation (PDE) is derived for the Green's function ψ [11], from which a concentration profile is obtained. This equation has the form of a nonlinear Schrödinger equation, reminiscent of equations used to model a confined

Bose gas [24]. Numerical solutions for the concentration profile, computed using a commercially available PDE-solver, are compared with the experimental profiles. We find good agreement when the number of packed chains is large, suggesting that mean-field-type regimes are probed in the experiments.

3.4 Experiment

The nanoslits were fabricated in fused silica wafers (HOYA corporation USA) using the protocol provided in Reisner *et al.* [26]. Our device comprises two U-shaped microchannels, coupled to sandblasted loading reservoirs, spanned by an array of nanoslits (Fig. 3.2(a)). The nanoslits are 75 μ m long, either 2 μ m or 10 μ m wide, with a height dimension of 300 nm. The nanoslits terminate in the array center in blunt-ended gaps. In a second lithography step, we etch a thin (30 nm) slit over the blunt-ended gaps, creating an array of semipermeable barrier structures that permit fluid flow, but are sufficiently thin to trap DNA. The chips were bonded to fused-silica coverslips to form channels of uniform silica surface chemistry. The chips were then wet with a 1×TE buffer and degassed in a vacuum chamber for 12 hours prior to use. Additional 1×TE buffer with λ -DNA (New England BioLabs), stained with YOYO-1 (intercalation ratio of 1:10), was then loaded into the devices. To prevent photobleaching and photonicking of DNA, the loading buffer includes 2% β -mercaptoethanol. Our imaging setup is based on a Nikon Eclipse Ti microscope with a 100×N.A. 1.49 oil immersion objective (Nikon), a metal-halide lamp (Xcite) as an excitation source and a iXon EMCCD camera (Andor). A schematic of a chip is shown in Fig. 3.2(a).

We first load DNA solution into reservoirs 2 and 3 (Fig. 3.2(a)). Pneumatic pressure, generated by a nitrogen flow applied at reservoir 2 and 3, is used to introduce DNA into a microchannel arm. Pressure applied at reservoirs 1–4 is then used to drive DNA from the microchannel into the nanoslit array, gradually filling the nanoslits with DNA (Fig. 3.2(b-c)). Figure 3.2(d) shows a kymograph representation of the growth of a packing as individual molecules are added one by one. The kymograph representations are constructed by first averaging the intensity of each image in the direction transverse to the nanoslit axis, and then reslicing, displaying time along the y-axis and longitudinal position along the x-axis. The fluid velocity at each applied pressure is measured by extracting the speed of a free moving DNA molecule v_{coil} in a nanoslit during the packing formation (for example, by performing a linear fitting to a free molecule trajectory, as shown in Fig. 3.2(d)).

Once a prescribed number of DNA are introduced into the nanoslit, compression is initiated against the barrier (Fig. 3.2(e)). Pneumatic pressure is applied to the two outer reservoirs of the device where no DNA solution is loaded (e.g., reservoirs 1 and 4), ensuring that no additional DNA

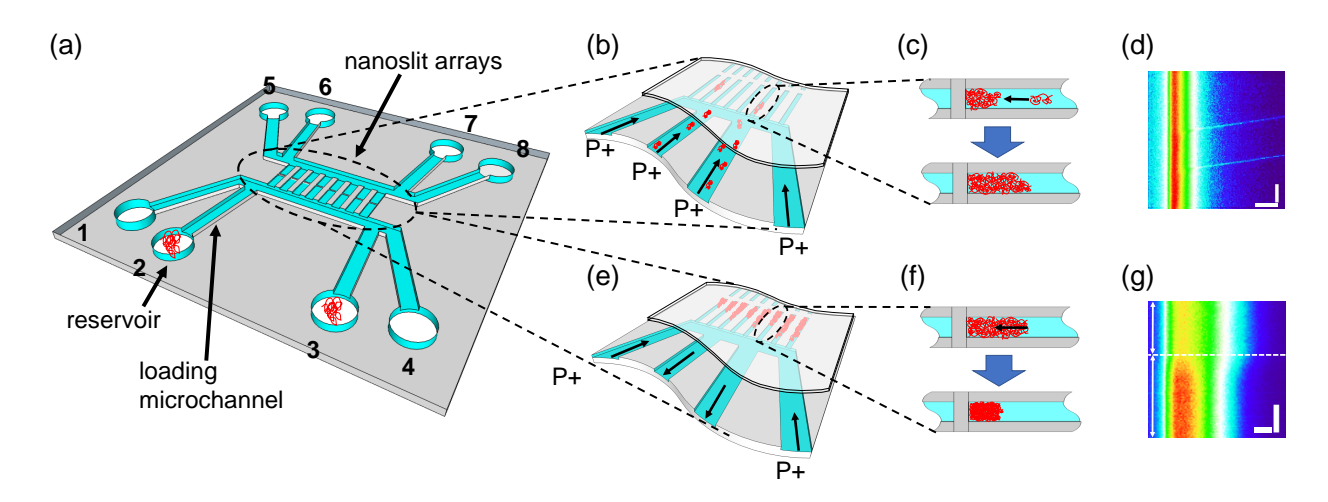


Figure 3.2: (a) Schematic showing the chip layout. DNA molecules are initially loaded in reservoirs 2 and 3 and (b) driven into the slit array by symmetric application of pneumatic pressure to all reservoirs. (c) A packing of chains is built up in each slit with (d) a kymograph showing individual chains being driven down the slit into the packing (the vertical scale bar is 1 s while the horizontal scale bar is 4 μ m). Once the packing is complete, pressure is released at reservoirs 2 and 3, so that (e) the overall compression of the packing can be tuned by varying pressure applied at reservoirs 1 and 4 without introducing new molecules. (f) Increasing pressure by a fixed increment will increase in packing density with (g) a kymograph showing a transition for 79 ± 6 DNA from 96 mbar to 151 mbar (the vertical scale bar is 2 s and the horizontal scale bar is 2 μ m).

will be introduced into the nanoslit during compression (and the molecule number is conserved) as shown in Fig. 3.2(e-g). Compression is initiated at a low pressure (~ 25 mbar). When pressure is applied, there is a short transient process during which chains throughout the nanoslit accumulate at the barrier (Fig. 3.2(f-g)). Eventually the packing reaches a steady-state where the concentration profile has a stable extent and structure (Fig. 3.2(g)). We then acquire images for about 10 s to achieve a satisfactory signal-to-noise ratio and, thus, a robust measurement of the profile structure. The pressure is then increased to achieve higher packing densities, and the process iterated over a range of pressures.

The key observable in the assay is the variation of polymer concentration with position along the channel axis. This longitudinal concentration profile is extracted directly from the raw video microscopy images. First, we isolate the portions of the video where the packing is steady at a given pressure (corresponding to 200-300 frames). Next, we select a region that captures thefluorescence intensity from the polymers. Then, on a frame-by-frame basis, we sum the packing intensity over the direction transverse to the channel axis to create a profile of concentration versus longitudinal position. Finally, we average the longitudinal profile over all steady-state frames; the error in the averaged concentration is determined from the error-of-the-mean arising from intensity fluctuations between frames. The total intensity of the profile is proportional to the number of DNA molecules. We obtain the number of DNA N in the packing by dividing the total intensity of the packing by the intensity of one molecule (extracted before the chain is integrated into the packing). Lastly, we normalize the resulting intensity profile to the total intensity I_{tot} (summed over all pixels in the profile) and the pixel size Δx_{pix} . The normalization is performed separately for each increment in compression of a fixed number of polymer coils, accounting for any effects of photobleaching. The normalized longitudinal concentration profile is denoted C'.

Figure 3.3 shows kymograph representations (Fig. 3.3(a), (c), (e), (g), and (i)) and resulting time-averaged longitudinal concentration profiles (Fig. 3.3(b), (d), (f), (h), and (j)) following compression. The DNA packing is compressed at different pressures, i.e., 27 mbar, 47 mbar, 96 mbar, 151 mbar and 196 mbar, corresponding to v_{coil} values of 1.13 μ m/s, 1.96 μ m/s, 4.01 μ m/s, 6.30 μ m/s and 8.18 μ m/s. The displayed kymographs do not show the whole event continuously, but only the steady-state portions. Qualitatively, the profiles ramp towards the barrier and then drop at the barrier edge; the scale over which the intensity falls-off at the barrier edge is governed by the specific boundary conditions imposed at the slit-barrier and the optical resolution (e.g., width of the point-spread function (PSF)) which will be discussed below.

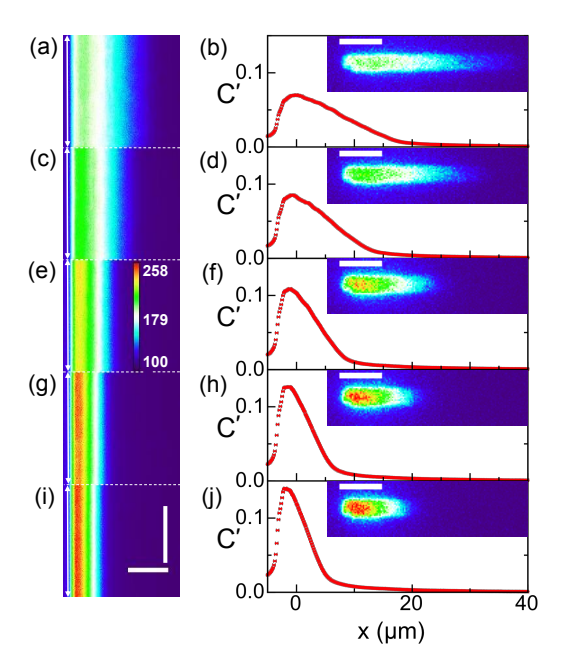


Figure 3.3: Kymographs (a, c, e, g and i) and corresponding concentration profiles (b, d, f, h and j) obtained from averaging the kymographs over 20 s when the packing, incorporating 79 ± 6 DNA molecules, has reached steady-state. The profiles were taken for a range of applied pneumatic pressures, each corresponding to a different fluid velocity. A measure of the fluid velocity in the slit is obtained from the velocity v_{coil} of free DNA coils moving in the slit for the given pressure. The applied pressures are (a-b) 27 mbar (corresponding to $v_x = 1.13 \,\mu\text{m/s}$), (c-d) 47 mbar (1.96 μ m/s), (e-f) 96 mbar (4.01 μ m/s), (g-h) 151 mbar (6.30 μ m/s), and (i-j) 196 mbar (8.18 μ m/s). The intensity profiles are normalized so that the total area under each curve is one. The horizontal scale bar is $10 \,\mu\text{m}$; the vertical scale bar is 2 s for the kymographs. Insets (b), (d), (f), (h), and (j) show corresponding 2D intensity profiles with a scale bar of $5 \,\mu\text{m}$.

Theory

3.5 Theory

3.5.1 Onsager's Variational Method Using a Two-Fluid Model

The shape of the concentration profile encodes information about how the polymer solution responds to external hydrodynamic forcing. For polymer concentration above the overlap threshold, the polymer packings exist in a semi-dilute solution regime. The overlap concentration for a slit-confined solution is given by Daoud *et al.* [6]

$$c_* = \frac{n}{\pi h r_g^2},\tag{3.1}$$

where n is the number of Kuhn length segments in one molecule and r_g is the gyration radius of a single slit-confined molecule [5], and h is the slit height (the factor of π is used for a more precise estimate of the coil area). We show that the packing concentration is above overlap over most of the measured profile (Fig. 3.6(a)). In addition, we observe that the longitudinal concentration profiles of the polymer packings are linear ramps (Fig. 3.3), a characteristic indicative of mean-field behaviour if the friction factor is proportional to packing concentration, as observed for single chains [17, 18]. These results motivate development of a systematic theory, based on classic mean-field assumptions, to describe compressed DNA solutions.

M. Doi has demonstrated that the Onsager principle of minimum dissipation is a powerful, general approach for constructing kinetic equations in soft-matter systems [8]. This approach transparently establishes the connection between a system's equilibrium free energy and resulting non-equilibrium behaviour under applied forcing provided a dissipation function can be constructed. In addition, supplemented by a two-fluid type modelling approach [10], the Onsager approach incorporates subtle details regarding the coupling between hydrodynamics and polymer dynamics. Here we use the Onsager principle to construct evolution equations for the evolving polymer concentration assuming mean-field and develop steady-state solutions satisfied when the polymer solution is driven against a barrier under constant external flow.

Our system comprises a solvent phase, of velocity \mathbf{v}_s , and a polymer phase, of velocity \mathbf{v}_p . The polymer has concentration c (Kuhn segments per unit volume) and polymer volume fraction ϕ . The polymer volume fraction is very small for our experimental system, on the order of $\phi \sim 0.001$. Therefore the average solution velocity

$$\mathbf{v} = \phi \mathbf{v}_n + (1 - \phi) \mathbf{v}_s \approx \mathbf{v}_s. \tag{3.2}$$

Theory Theory

Following M. Doi's version of the Onsager approach [8], we construct a Rayleighian $R = \Phi + \dot{A}$, where Φ is an energy dissipation functional and \dot{A} is the rate of change of free energy. The dissipation comprises two terms: Φ_{PS} , which is the dissipation arising from the relative motion of the polymer and solvent, and Φ_H , which is a purely "hydrodynamic" dissipation arising from velocity gradients. The first term Φ_{PS} can be written

$$\Phi_{PS} = \frac{1}{2} \int \zeta (\mathbf{v}_p - \mathbf{v})^2 d\mathbf{r}, \tag{3.3}$$

where ζ is a friction coefficient that is proportional to the polymer concentration c [17, 18]. The second term Φ_H can be written

$$\Phi_H = \frac{\eta}{4} \int \left[\nabla \mathbf{v} + (\nabla \mathbf{v})^t \right]^2 d\mathbf{r}, \tag{3.4}$$

where η is the solution viscosity, $\nabla \mathbf{v}$ is the velocity gradient tensor, and t indicates the transpose matrix.

For a mean-field polymer theory with ground-state dominance, the free energy [11]

$$A = k_B T \int \left(\frac{a^2}{6} |\nabla \psi|^2 + \frac{\nu}{2} |\psi|^4\right) d\mathbf{r},\tag{3.5}$$

where a=2P is the Kuhn length (100 nm for DNA), ν is the excluded volume parameter, and ψ is the Green's function, related to polymer concentration by $c=|\psi|^2$, and k_BT is the thermal energy. The first term of Eq. 3.5 arises from entropy, whereas the second term is comparable to a potential arising from self exclusion in the mean-field approach. The excluded volume parameter is $\nu=a^2d$ where d is the effective chain width [26].

To obtain the Rayleighian, we first need to compute the time derivative of free energy A and add it to the energy dissipation functional Φ . The full Rayleighian also requires a third Lagrange multiplier constraint L to maintain solvent incompressibility, $\nabla \cdot \mathbf{v} = 0$ (a condition which arises naturally from the definition of \mathbf{v} in Eq. 3.2 and the conservation of ϕ). We do this by introducing a pressure $p(\mathbf{r})$ so that the Rayleighian becomes

$$R = \Phi + \dot{A} - L = \Phi + \dot{A} - \int p(\mathbf{r})(\nabla \cdot \mathbf{v})d\mathbf{r}.$$
 (3.6)

Theory Theory

The Onsager principle of minimum dissipation requires

$$\frac{\delta R}{\delta \mathbf{v}_p} = 0$$
 and $\frac{\delta R}{\delta \mathbf{v}} = 0.$ (3.7)

Computing these functional derivatives yields two equations:

$$\zeta(\mathbf{v}_p - \mathbf{v}) = -\psi^2 \nabla \left(\frac{1}{2\psi} \frac{\delta A}{\delta \psi} \right)$$
 (3.8)

and

$$\zeta(\mathbf{v}_p - \mathbf{v}) + \nabla \cdot \eta \left[\nabla \mathbf{v} + (\nabla \mathbf{v})^t \right] = \nabla p, \tag{3.9}$$

where

$$\frac{\delta A}{\delta \psi} = 2k_B T \left(-\frac{a^2}{6} \nabla^2 \psi + \nu \psi^3 \right). \tag{3.10}$$

Equations 3.8 and 3.9 describe constraints on the behaviour of the flow and the concentration profile. Of particular interest is Eq. 3.8, because it explicitly yields the Green's function if the velocities are given.

We will work from now on with Eq. 3.8. Under steady-state compression, we assume the average velocity of the polymer $\mathbf{v}_p = 0$. Furthermore, as discussed, we assume the friction coefficient to be proportional to concentration: specifically $\zeta = \zeta_0 |\psi|^2$. Equation 3.8 then becomes

$$\zeta_0 \mathbf{v} = k_B T \nabla \left[\frac{1}{\psi} \left(-\frac{a^2}{6} \nabla^2 \psi + \nu \psi^3 \right) \right]. \tag{3.11}$$

The quantity ζ_0 is a constant that determines the slope of the linear ramp; we will later show how to use scaling arguments to estimate its value.

3.5.2 Reduction to One-Dimensional Theory

As the nanoslit height ($h=300\,\mathrm{nm}$) is small compared to the length and width dimensions ($l=75\,\mu\mathrm{m}$ and $w=2\,\mu\mathrm{m}$), we argue the problem reduces to a quasi-1D case. We orient the channel axis along x, the width dimension along y and the vertical dimension along z. To transform our 3-D equations into a system of 1-D equations, we assume separability of the functional dependence on the lateral coordinates x and y and the vertical coordinate z. We also assume that the flow is strictly parallel to the channel (x) axis, leading to

$$\psi(\mathbf{x}) = f(z)\psi_{xy}(x,y) \text{ and } \mathbf{v}(\mathbf{x}) = g(z)(v_x, 0, 0).$$
 (3.12)

Theory Theory

We expect only weak variation of ψ with y, as the width dimension is significantly larger than the vertical dimension, so in addition we argue $\psi_{xy}(x,y) \equiv \psi_x(x)$. We approximate the function f(z) by the transverse concentration profile appropriate for a confined Gaussian chain [11]

$$f(z) = \sqrt{\frac{2}{h}} \sin \frac{\pi z}{h}.$$
 (3.13)

We assume a Poisseuille velocity profile in the transverse direction, with v_x the constant average flow-velocity along the channel

$$g(z) = \frac{6}{h^2}(h - z)z. {(3.14)}$$

Replacing ψ and \mathbf{v} in Eq. 3.11 with the expressions in Eq. 3.12–3.14 and integrating over y and z, we obtain

$$\zeta_0 v_x = k_B T \frac{\partial}{\partial x} \left[\frac{1}{\psi_x} \left(-\frac{a^2}{6} \frac{\partial^2}{\partial x^2} \psi_x + \frac{\nu}{hw} \psi_x^3 \right) \right], \tag{3.15}$$

where w is the slit width. Since v_x is a constant, we may integrate both sides of Eq. 3.15 with respect to x and then multiply both sides by ψ to obtain

$$\epsilon \psi_x + \zeta_0 v_x x \psi_x = k_B T \left(-\frac{a^2}{6} \frac{\partial^2}{\partial x^2} \psi_x + \frac{\nu}{hw} \psi_x^3 \right). \tag{3.16}$$

This is now an eigenvalue problem with the eigenvalue ϵ arising from the integration.

To convert Eq. 3.16 to dimensionless form, we introduce the variables

$$C \equiv \frac{\psi_x^2}{c_* w h}$$
 and $\Psi \equiv \frac{\psi_x}{\sqrt{c_* w h}}$. (3.17)

Using these definitions, Eq. 3.16 becomes

$$E\Psi = -\xi^2 \frac{\partial^2 \Psi}{\partial x^2} + \Psi^3 + mx\Psi, \tag{3.18}$$

where

$$E \equiv \frac{\epsilon}{k_B T \nu c_*}, \ \xi^2 \equiv \frac{a^2}{6\nu c_*} \text{ and } m \equiv -\frac{\zeta_0 v_x}{\nu k_B T c_*}. \tag{3.19}$$

We will refer to Eq. 3.18 as the 'Linear Ramp Concentration PDE' (LRCPDE).

To compare with experiment, firstly we must note that our experimental profiles, normalized to one, have a different normalization than Eq. 3.18. This issue requires care as Eq. 3.18 is non-linear and normalization rescales the underlying equation parameters. The normalized profile $C' = (c_* wh/Nn)C$. Thus, the physical parameters E, ξ and m, appearing in Eq. 3.18, are related

Theory

to the corresponding parameters E', ξ' and m' obtained by fitting to the normalized experimental profiles via

$$E = E'/\eta, \quad \xi^2 = \xi'^2/\eta \text{ and } m = m'/\eta$$
 (3.20)

with the conversion factor $\eta \equiv (c_*wh/Nn) = (w/Nr_g^2\pi)$. Secondly, we need to relate the average flow velocity v_x to the velocity $v_{\rm coil}$ of a single free coil determined from experiment. The coil velocity can be estimated by averaging the Poisseuille flow over the chain concentration profile [34]. Using Eq. 3.13 to model the chain profile, we find $v_{\rm coil} = (1+3/\pi^2)v_x \approx 1.3v_x$. The coil velocity is a little higher than the average flow velocity because polymers are concentrated at the channel center.

3.5.3 Rescaling and Numerical Solution

The LRCPDE is of the same form as the Gross-Pitaevskii equation for a linear ramp potential [24], which describes the ground state of a quantum system of identical bosons. One approach for obtaining numerical solutions of the LRCPDE is to turn on the cubic (nonlinear) term adiabatically, starting in the ground-state of the linearized equation (simply the Schrödinger equation). Another approach, which is faster and gives equivalent results, is to convert the LRCPDE to a time-dependent equation by adding a $\partial\Psi/\partial t$ term and finding the LRCPDE solution as a long-time limit of the modified time-dependent system.

Solutions to the LRCPDE have a ramp-like character and can be divided into three regimes, as shown in Fig. 3.4: (1) a tail corresponding to low concentration ($\Psi^2 \sim 10^{-1}$ and lower) where the nonlinear term is negligible, (2) a linear ramp where the nonlinear term is dominant, and (3) a boundary region determined by the specific boundary conditions imposed at the slit barrier. The parameter ξ is the correlation length, which sets the length scale in the boundary and the tail regions. If the excluded-volume term is dominant, then we may omit the derivative in the LRCPDE, giving an explicit equation for the linear regime:

$$C = \Psi^2 = mx - E = m(x - x_o). \tag{3.21}$$

The parameter m is the ramp slope and $x_0 = E/m$ is the ramp x-intercept. In quantum language, this is known as a Thomas-Fermi approximation [24].

The LRCPDE can be rescaled by adopting the reduced variables [24]

$$\widetilde{x} = \frac{m^{1/3}}{\xi^{1/3}} \left(x - x_0 \right) \tag{3.22}$$

48 Theory

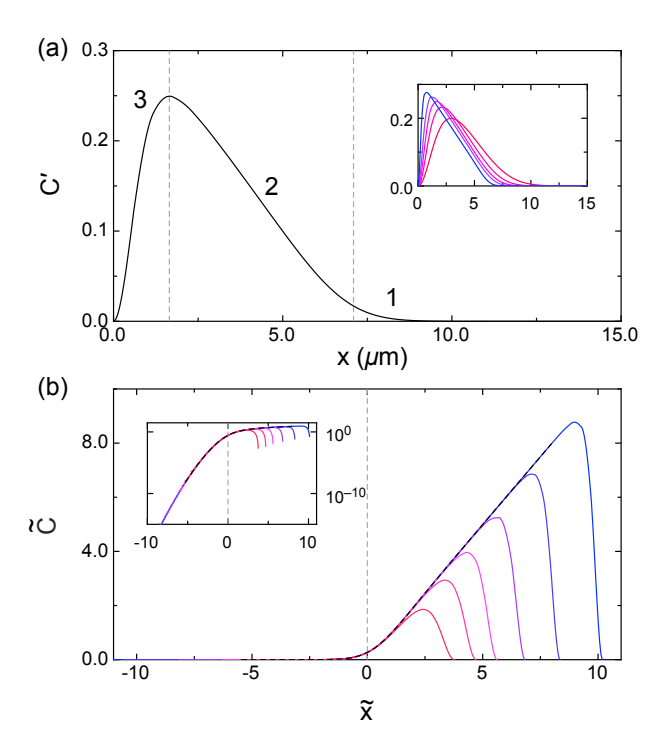


Figure 3.4: (a) An example solution to the LRCPDE, obtained using the boundary condition $\Psi^2=0$ at x=0, for $m=0.05\,\mu\mathrm{m}^2$ and $\xi=0.1\,\mu\mathrm{m}$. Dashed grey lines separate the three regimes: (1) tail, (2) ramp, and (3) boundary region. Inset shows several solutions to the LRCPDE for the same value of m but increasing ξ (from blue to pink). (b) Additional solutions to the LRCPDE for varying m and ξ (from blue to pink), rescaled according to Eq. 3.22 and 3.23 (and flipped along the y-axis). The master curve, solution to Eq. 3.24, is shown in dashed black. A dashed grey line separates the tail and ramp regions. The inset shows the same curves with log-linear axes.

and

$$\widetilde{\Psi} = \frac{\Psi}{m^{1/3} \xi^{1/6}}.$$
(3.23)

Equations 3.22 and 3.23 lead to the rescaled LRCPDE:

$$-\frac{\partial^2 \widetilde{\Psi}}{\partial \widetilde{x}^2} + \widetilde{\Psi}^3 + \widetilde{x}\widetilde{\Psi} = 0.$$
 (3.24)

The effect of varying the eigenvalue E is highlighted in Eqs. 3.21 and 3.22: varying E varies x_0 and translates the profile along the x-axis. In particular, $\widetilde{x}=0$ corresponds to the position $x=x_0$. Figure 3.4 shows the effect of rescaling numerical solutions of the LRCPDE according to Eqs. 3.22 and 3.23. The curves collapse with deviations from the master envelope occurring only in a small region near the boundary. Solving the LRCPDE with E=0, and without imposing specific boundary conditions at the barrier, produces a master-curve that describes the envelope produced by the collapse of the rescaled solutions. Note that we present non-rescaled concentration profiles/numerical solutions with the tail towards the right, and flip the profiles/solutions about the y-axis when we rescale them, so that the tail points towards the left and the slope is positive.

3.6 Theory Compared to Experiment

Before we compare experimental data to theory, we must first consider the effect of the PSF, which has two components. The first arises from fluorescence emitted by a point-source that is directly transmitted through the device bonding-lid, and is described by a standard Airy disk:

$$PSF(r) = I_0 \left(\frac{2J_1(r/r_0)}{r/r_0}\right)^2,$$
 (3.25)

where J_1 is the Bessel function of the first kind of order one, $r=\sqrt{x^2+y^2}$ is the radial distance from the optics axis in the focal plane, and r_0 is an effective width parameter of the Airy disk. Specifically, $r_0 = \frac{\lambda N}{\pi}$, where λ is the wavelength of observed light, and N=R/d is the f-number, where R is the observation distance and d is the aperture diameter. To calibrate the Airy-disk response for this system (e.g., determine r_0), we measured the intensity profile of an object below the diffraction limit (a 75 nm fluorescent bead, see Fig. 3.5(a)). We then convolved the Airy-disk with a 75 nm diameter disk representing the bead extent, and fitted the resulting profile to the bead intensity profile, yielding $r_0=0.22~\mu{\rm m}$.

Because our observables are one-dimensional profiles along the channel axis, we use a one-

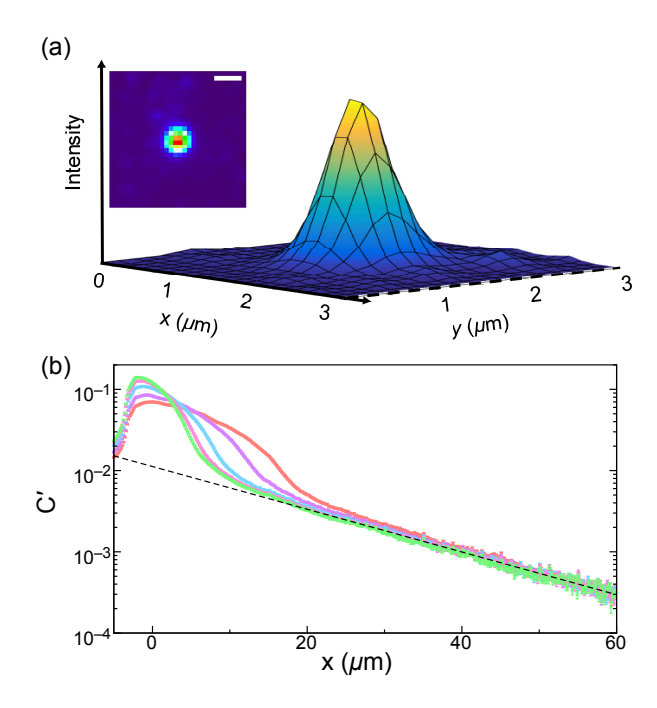


Figure 3.5: (a) Intensity profile of a 75 nm fluorescent bead imaged with a $100 \times N.A.$ 1.49 objective. The scale bar on the coloured micrograph inset is $1 \mu m.$ (b) Log-linear plot of concentration profiles, taken for different pressures, in a $2 \mu m$ wide slit for a packing containing 79 DNA molecules (x-axis linear, y-axis log). The pale-red curve corresponds to a pressure of 27 mbar, purple curve 47 mbar, blue-curve 96 mbar, pink curve 151 mbar and green curve 196 mbar. The profile tails far away from the slit-barrier fit well to an exponential function (dashed-black curve).

dimensional projection of the Airy PSF to form a line PSF. The line LSF can be obtained from the Airy PSF by integration, and is given by [37]

$$LSF_{Airy}(x) = \int_{-\infty}^{+\infty} I_0 \left[\frac{2J_1((x^2 + y^2)^{1/2}/r_0)}{(x^2 + y^2)^{1/2}/r_0} \right]^2 dy$$

$$= I_0' \left(\frac{H_1(2x/r_0)}{(x/r_0)^2} \right),$$
(3.26)

where H_1 is a first-order Struve function.

The second PSF component arises from fluorescence emitted by a transverse segment of the slit that is not directly transmitted, but instead is guided down the slit. This wave-guiding effect is apparent in the long-range intensity tails far away from the DNA packing, as shown in Fig. 3.5(b). These tails are symmetrically distributed around the packing, are independent of packing concentration, and have an exponential character. We attribute these exponential tails to the exponential attenuation of light in a dielectric wave-guide due to scattering loss [15]. To account for the wave-guiding effect, we introduce a second component to the line PSF that has the form of a symmetric exponential:

$$LSF_{\text{waveguide}}(x) = A \exp(-a|x|). \tag{3.27}$$

The constant a describes the decay length of the exponential tail; A represents the fraction of light that is wave-guided, with the absolute value ensuring that the wave guiding effect is symmetric on both sides of the line source. We find both a and A are independent of packing density (applied pressure).

To compare our experimental data with theory, we generated numerical solutions of the LR-CPDE for different values of ξ and m, with the time-dependent equation method, using a commercially available PDE solver (FlexPDE). We then convolved these numerical solutions with a line-spread function LSF that is the sum of the Airy and waveguide contributions:

$$LSF(x) = LSF_{Airy}(x) + LSF_{waveguide}(x).$$
(3.28)

The experimental concentration profiles were then fitted to these convolved numerical solutions (using Matlab's lsqcurvefit). There are five parameters to be determined from the fit: ξ , m, A, a and the overall translation along the x-axis, x_0 . We omitted the boundary portion of the profile when performing the fits; firstly, because the exact boundary condition at the barrier is uncertain, due to the complex geometry of the channel at the barrier and because the unidirectional-flow approximation breaks down near the barrier; secondly, because the boundary region does not reflect

universal characteristics of the profile (the tail and ramp portions of the profile do not depend on the specific boundary condition imposed at the barrier, e.g., see Fig. 3.4). If we omit the boundary portion, then we have freedom to set E=0 when computing the solution. Note that x_0 will be determined uniquely only if a boundary condition is imposed at a specific position (i.e., if a boundary condition is imposed, the profile will not be invariant under translation, fixing x_0).

Figure 3.6(a) compares the experimental longitudinal concentration profiles with convolved theoretical calculations for a packing that comprises $N=79\pm 6$ molecules measured at five different pressures (for clarity, curves for the three lowest pressures are shown). The profiles taken for different pressures were fit together, with the values of ξ , A and a set to the same value for all five curves, while m and x_0 are determined independently for each curve. The concentration in Fig. 3.6(a) is plotted in units of the overlap concentration; note that C>1 for most of the curves, so the packing is really in a semi-dilute solution (as opposed to dilute regime) and the use of a solution model is justified. This model describes the results quite well.

Figure 3.6(b) presents the fitted slope of the linear regime (m, Eq. 3.21) plotted versus v_{coil} . We find that m has the linear dependence on v_{coil} predicted by Eq. 3.19; the fitted slope $m/v_{\text{coil}} = 0.476 \pm 0.001 \, \text{s}/\mu\text{m}^2$. To compare to the m-value predicted by theory (e.g., Eq. 3.19), we need to estimate ζ_0 and find c_* using Eq. 3.1. The maximum possible value of ζ_0 is the friction factor of a single Kuhn segment ($\approx 6\pi\eta a$). This is necessarily an overestimate due to hydrodynamic screening. If we argue that hydrodynamics are screened over the slit height h, then the friction factor is simply the friction factor for a blob of extent h times the number of blobs per unit volume, or $\zeta = (6\pi\eta h)(C/n_H)$, where n_H is the number of Kuhn segments in a blob [11]. We estimate the number of segments per blob by assuming that the blobs obey Flory scaling, e.g., $n_H = h^{5/3}/(Pd)^{1/3}a$, giving

$$\zeta_0 \approx 6\pi \eta a (Pd)^{1/3} / h^{2/3}.$$
 (3.29)

Equation 3.29 gives $\zeta_0=421\,\mathrm{nm}$ mPa s (using $\eta=1\,\mathrm{mPa}$ s, $P=50\,\mathrm{nm}$, and $d=20\,\mathrm{nm}$, appropriate for our buffer [21]). To estimate the overlap concentration c_* , we need to determine the radius of gyration of a single slit confined λ -DNA molecule. For this, we use simulation results for the slit-confined chains summarized by Dai et~al. [5]. Figure 7 in Dai et~al. gives $r_g=1.5r_g^{\mathrm{bulk}}$ for $h=300\,\mathrm{nm}$, where r_g^{bulk} is the bulk (unconfined) gyration radius of λ -DNA. In addition, from their simulations, they report $r_g^{\mathrm{bulk}}=392\times d^{0.19}$, giving $r_g=1040\,\mathrm{nm}$ (using $d=20\,\mathrm{nm}$). Taking the dye-adjusted contour of λ -DNA to be $20\,\mu\mathrm{m}$ [26], we find n=200, so that Eq. 3.1 gives $c_*=196\,\mu\mathrm{m}^{-3}$. Equation 3.19 then gives $m/v_{\mathrm{coil}}=2.03\,\mathrm{s}/\mu\mathrm{m}^2$ ($\nu=20\,\mathrm{nm}\times(100\,\mathrm{nm})^2$ and $T=293\,\mathrm{K}$), which is larger than the experiments by a factor ≈ 4 . We attribute the discrepancy to an absence of complete hydrodynamic screening by the blobs, since the factor of 6π in the definition of

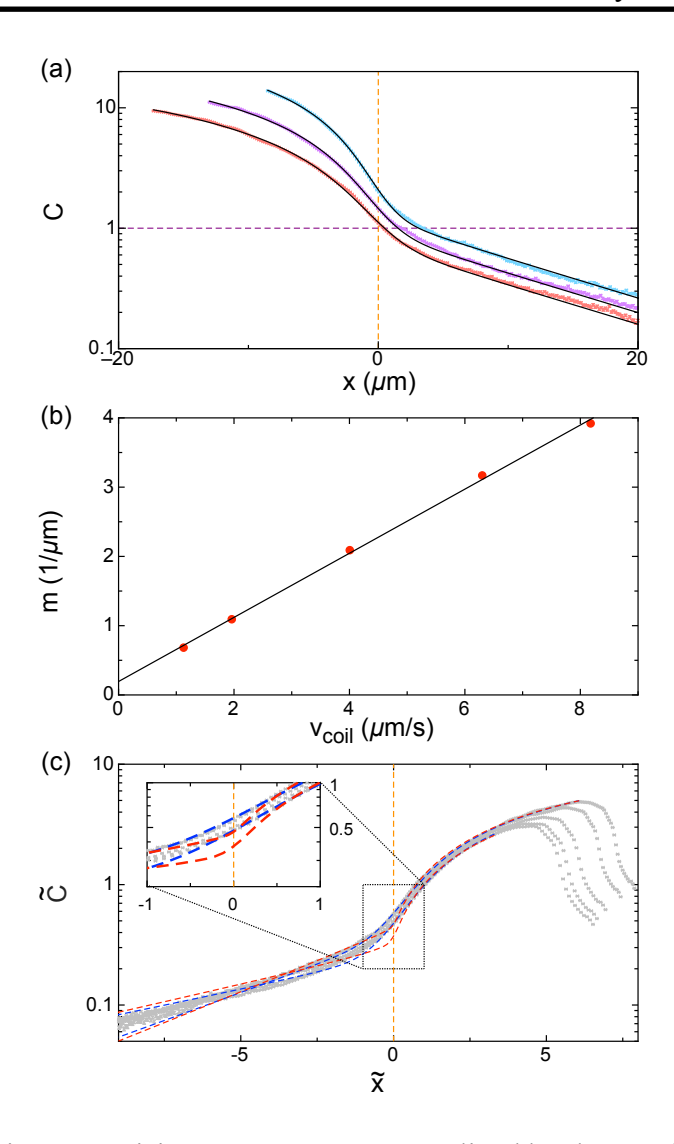


Figure 3.6: (a) A packing comprising 79 ± 6 DNA, normalized by the overlap concentration, with fitted theory for pressures of 27 mbar (pale red curve, corresponding to $v_{\rm coil}=1.13~\mu \rm m/s$), 47 mbar (purple curve, $1.96~\mu \rm m/s$), and 96 mbar (blue curve, $4.01~\mu \rm m/s$). Theory is shown in black for each pressure. Overlap concentration is shown in dashed purple and x_0 is shown in dashed orange. Data was taken in a 2 $\mu \rm m$ slit. (b) The fitted slope parameter m (red) for the three previous pressures, as well as for 151 mbar (6.30 $\mu \rm m/s$) and 196 mbar (8.18 $\mu \rm m/s$), as a function of flow speed measured by $v_{\rm coil}$, and linear fit (black). Error-bars on fitted m values are smaller than the point size. (c) The same data with all 5 pressures shown in grey, rescaled according to Eq. 3.22 and 3.23, plotted with convolved theory (blue-dashed) and a simple line convolved with the same LSF model (red-dashed). The convolved theory and convolved line correspond to the best fit to the highest and the lowest pressures data (with curves taken for other pressures lying between the two lines). The inset emphasizes that, in the region about $\widetilde{x}=0$ (indicated in dashed orange line), the full mean-field model gives improved agreement to the collapsed experimental profiles (as compared to the simple convolved line model).

 ζ_0 assumes that the blobs act as hard spheres. The fitted correlation length is $\xi=3.960\pm0.052\,\mu\text{m}$, which is of the order of the end-to-end length of a single coil ($\approx\sqrt{6}r_g=2.5\,\mu\text{m}$).

Figure 3.6 (c) shows the same experimental profiles and convolved theoretical fits rescaled according to Eqs. 3.22 and 3.23 with the m and ξ parameters determined from the fit of each profile to theory. For clarity, we plot the theory only for the highest and lowest pressures, which bracket the range of theoretical fits corresponding to the five profiles. The rescaling collapses both the experimental profiles and their corresponding theoretical fits. The collapse is not perfect, but this is expected, due to the influence of the line-spread function; the convolved theory and experiment show a similar (small) degree of deviation from perfect collapse. In addition, in Fig. 3.6(c), we check whether the full mean-field model is better than the approximate linear model at describing the collapsed profiles. The linear model, convolved with Eq. 3.28 (red-dashed curve), agrees with the experimental profiles and full mean-field theory for $\tilde{x} > 1$, but deviates from the collapsed experimental profiles for \tilde{x} values close to the origin. In contrast, the mean-field description (blue-dashed curve) provides a good description of the experimental data for $\tilde{x} > 1$ and \tilde{x} values close to the origin.

We have also explored the effect of varying molecule number N on the packing profiles. Figure 3.7 shows profiles taken for different N and different pressures fitted to the convolved theory and then rescaled. As above, we show the best fit to the convolved theory for the highest and lowest pressures. At high N (Fig. 3.7(a-b)), the collapse works well, and the collapsed profiles agree with the mean-field theory. As N decreases (Fig. 3.7(c-d)), the collapse degrades for $\tilde{x} < 0$, and the mean-field theory falls systematically below the collapsed profiles. The deviation from the mean-field theory appears to be associated with a decrease in the overall packing concentration. In particular, for the low N profiles, the profiles at higher pressure agree better with the mean-field model. We examined packing profiles in larger (10 μ m wide) slits (Fig. 3.7(e-f)), finding similar behaviour.

3.7 Discussion and Conclusions

We have developed a nanofluidic system for creating confined polymer solutions and studying their response to compressive hydrodynamic forcing against a barrier. A Gross-Pitaevskii type equation was derived to describe the 1-D chain packing profile, treating the flow-induced DNA compression as a sedimentation problem, and using mean-field and ground-state dominance assumptions in the context of Onsager dissipation minimization. The mean-field theory works well when N is sufficiently high. Experimental data, rescaled according to Eqs. 3.22 and 3.23, exhibit striking

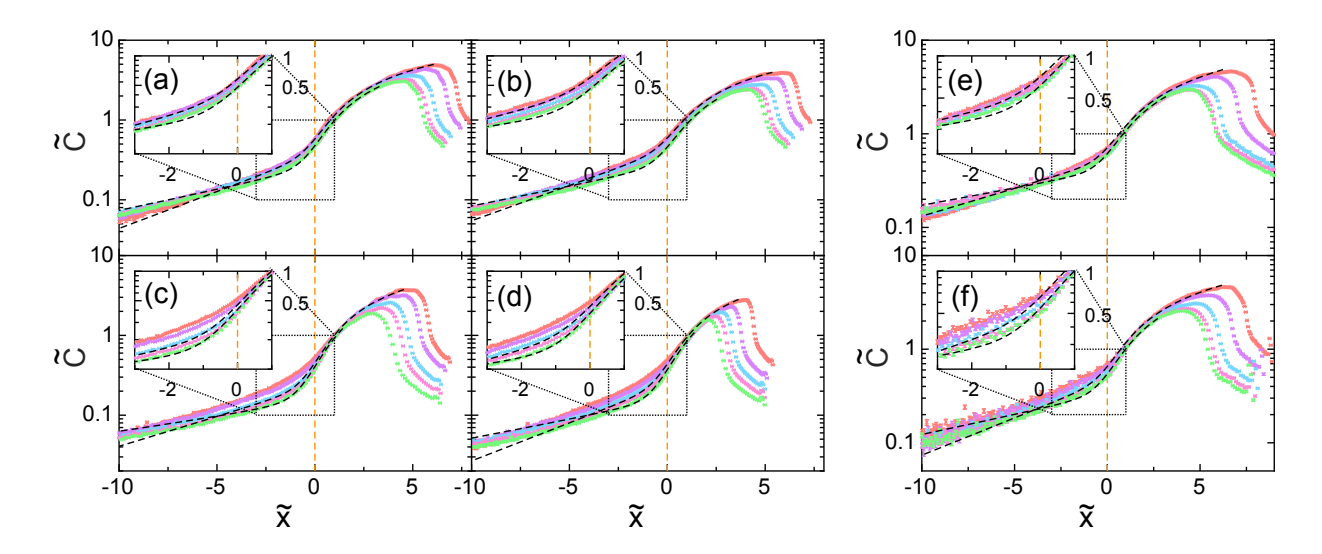


Figure 3.7: Experimental packing profiles for $2 \,\mu \mathrm{m}$ slits (a-d), and for $10 \,\mu \mathrm{m}$ slits (e-f), rescaled according to fitting parameters following Eq. 3.22 and 3.23: (a) $N = 79 \pm 6 \,\mathrm{DNA}$, (b) $60 \pm 6 \,\mathrm{DNA}$, (c) $57 \pm 9 \,\mathrm{DNA}$, (d) $50 \pm 5 \,\mathrm{DNA}$, (e) $154 \pm 28 \,\mathrm{DNA}$ and (f) $78 \pm 19 \,\mathrm{DNA}$. In each plot $p \approx 25 \,\mathrm{mbar}$ (pale red), 50 mbar (purple), 100 mbar (blue), 150 mbar (pink) and 200 mbar (green), resulting in flow speeds ranging from $1 \,\mu \mathrm{m/s}$ to $22 \,\mu \mathrm{m/s}$. The dashed-black curves are rescaled best fits to mean-field theory at the highest and lowest pressures.

data collapse (despite the interference of the LSF), and agree well with the mean-field theory (LR-CPDE, Eq. 3.18) convolved with the LSF, in Fig. 3.7). As N decreases, however, the data collapse is weaker, and the correspondence with mean-field theory breaks down. In particular, with fewer confined DNA molecules and a lower applied pressure (e.g., Fig. 3.7 (c-d) and (f)), the discrepancy between theory and rescaled experimental data becomes pronounced in the tails.

The very good agreement with mean-field theory and experiments—in the profile tails—is, perhaps, surprising (see Fig. 3.6(a)). In particular, we did not expect a bulk mean-field regime to exist at concentrations so close to overlap; in addition, the large correlation length is inconsistent with a bulk regime, with the bulk correlation length being an order of magnitude lower. One explanation for these observations hinges on the existence of a special transition regime. In de Gennes' classic theory for confined flexible polymer solutions [6], such a transition bridges the dilute and bulk regimes where the correlation length is larger than the slit height. Such a transition might be expected for solutions of semiflexible chains, as for single semiflexible chains in strong confinement [30]. Note that the transition regime predicted by Sakaue for a single confined semiflexible chain is also a mean-field regime, but with a larger correlation length. Thus, one explanation for the agreement of mean-field theory and experiments here—in the tails, and the larger correlation

length, is that our assay probes the transition for confined solutions of semiflexible chains.

In Sakaue's theory for single confined semiflexible chains, both "fluctuating" regimes with scalings analogous to flexible chain theory and mean-field regimes exist. The structure of the predicted scaling regimes as a function of chain size and confinement scale is complex. Moreover, for confined solutions, incontrast to single chains, the number of confined chains is an additional variable. We speculate that the departures from mean-field theory that we observe for lower N might arise when entering a transition regime that is no longer described by mean-field theory.

Further experiments varying the slit height, molecule number, and chain contour length could help to clarify these issues by (i) helping to provide a rigorous experimental basis for the theory of confined solutions, and (ii) identifying subtle cross-overs between scaling regimes. Our assay could be adopted for other polymer systems too, such as flexible synthetic chains and confined solutions of polymers having complex architecture (e.g., ring and branched polymers). The effects of varying the solvent (e.g., salt variation and addition of molecular crowders or multi-valent species to drive the coils into a globule regime) on the polymer conformation and packing profiles might also be valuable.

3.8 Supplementary Materials

Here we go through the full derivation of the Rayleighian and Equations 3.8 and 3.9 in the manuscript. The free energy is given in Equation 3.5 in the manuscript. To compute the time derivative of the free energy,

$$\dot{A} = \int \dot{\psi} \frac{\delta A}{\delta \psi} d\mathbf{r}. \tag{3.30}$$

We use the conservation of molecular contour $\dot{c} + \nabla \cdot (c\mathbf{v_p}) = 0$, and calculate $\dot{\psi}$ to be

$$\dot{\psi} = \frac{\partial \psi}{\partial c} \dot{c} = \frac{1}{2\sqrt{c}} \dot{c} = \frac{1}{\psi} \dot{c} = -\frac{1}{\psi} \nabla \cdot (\mathbf{v_p} \psi^2)$$
 (3.31)

Then, integrating by parts, we have

$$\dot{A} = -\frac{1}{2} \int \nabla \cdot (\mathbf{v_p} \psi^2) \left(\frac{1}{\psi} \frac{\delta A}{\delta \psi} \right) d\mathbf{r}$$
 (3.32)

$$= -\frac{1}{2} \int \mathbf{v_p} \cdot \mathbf{n} \left(\psi \frac{\delta A}{\delta \psi} \right) dA + \frac{1}{2} \int \psi^2 \mathbf{v_p} \cdot \nabla \left(\frac{1}{\psi} \frac{\delta A}{\delta \psi} \right) d\mathbf{r}. \tag{3.33}$$

The first term of equation 3.33 is evaluated over the surface, and vanishes since the boundary condition of our system is $\psi = 0$. The full Rayleighian is therefore

$$R = \Phi_{PS} + \Phi_{H} + \dot{A} - L$$

$$= \frac{1}{2} \int d\mathbf{r} \zeta (\mathbf{v}_{\mathbf{p}} - \mathbf{v}_{\mathbf{s}}) + \frac{\eta}{4} \int (\nabla \mathbf{v} + (\nabla \mathbf{v})^{t})^{2} d\mathbf{r} + \frac{1}{2} \int \psi^{2} \mathbf{v}_{\mathbf{p}} \cdot \nabla \left(\frac{1}{\psi} \frac{\delta A}{\delta \psi}\right) d\mathbf{r}$$

$$- \int p(\mathbf{r}) (\nabla \cdot \mathbf{v}) d\mathbf{r}.$$
(3.34)

The Onsager principle of minimum dissipation requires

$$\frac{\delta R}{\delta \mathbf{v}_p} = 0$$
 and $\frac{\delta R}{\delta \mathbf{v}} = 0$. (3.35)

Computing each functional derivative term by term yields

$$\frac{\delta\Phi_{PS}}{\delta\mathbf{v}_p} = -\frac{\delta\Phi_{PS}}{\delta\mathbf{v}} = \int \zeta(\mathbf{v_p} - \mathbf{v})d\mathbf{r},$$
(3.36)

$$\frac{\delta \Phi_H}{\delta \mathbf{v}} = -\int \nabla \cdot \eta \left[\nabla \mathbf{v} + (\nabla \mathbf{v})^t \right] d\mathbf{r}$$
 (3.37)

using integration by parts,

$$\frac{\delta \dot{A}}{\delta \mathbf{v}_{p}} = \frac{1}{2} \int \psi^{2} \nabla \left(\frac{1}{\psi} \frac{\delta A}{\delta \psi} \right) d\mathbf{r}$$
(3.38)

using integration by parts, and

$$\frac{\delta L}{\delta \mathbf{v}} = -\int \nabla p d\mathbf{r} \tag{3.39}$$

again using integration by parts. Therefore we obtain:

$$\frac{\delta R}{\delta \mathbf{v_p}} = \int d\mathbf{r} \zeta(\mathbf{v_p} - \mathbf{v}) + \frac{1}{2} \int \psi^2 \nabla \left(\frac{1}{\psi} \frac{\delta A}{\delta \psi} \right) d\mathbf{r} = 0$$
 (3.40)

which can be rewritten as Equation 3.8 in the manuscript, and

$$\frac{\delta R}{\delta \mathbf{v}} = -\int d\mathbf{r} \zeta(\mathbf{v}_p - \mathbf{v}) - \int \nabla \cdot \eta \left[\nabla \mathbf{v} + (\nabla \mathbf{v})^t \right] d\mathbf{r} + \int \nabla p d\mathbf{r} = 0$$
 (3.41)

which can be rewritten as Equation 3.9 in the manuscript.

Chapter 4

Conclusion

4.1 Summary of Key Results

We have developed an experimental device to study polymer solutions under confinement, based on a device used to study and manipulate single chains. The device contains an array of nanoslit inside which polymer molecules are packed; a barrier at the end of the slits traps the molecules while allowing solvent to flow through. We image the steady-state molecule packing compressed against the barrier and transform the videomicroscopy images into a one-dimensional polymer concentration profile along the slit longitudinal axis. We develop a theory based on the Onsager variational principle and mean-field type free energy to model the behaviour we observe. The theory yields a Schrödinger's equation governing the Green's function ψ related to concentration as $|\psi|^2 = c$. This equation has exactly the same form as the Gross-Pitaevskii equation with a linear ramp potential. We compute numerical solutions to this equation and fit them to our data. We find good agreement between theory and experiment, for high enough concentration.

Until now, while the physics of single polymer molecules, flexible and semiflexible, is well understood, polymer solutions have been overlooked, especially experimentally. We have reviewed Sakaue's study of single semiflexible polymers under confinement [30] and the study of Daoud *et al* of flexible polymers under confinement [6], and extended their theories to solutions of semiflexible polymers under confinement. In particular, we find that just like in some regimes of confinements for single semiflexible polymers, mean-field type scalings apply to our data. We also find a large correlation length (larger than confinement size) from fitting the data to the mean-field model. These findings mean that such a regime, with mean field scaling and high correlation length, must exist for semiflexible polymer solutions. And they lead us to conclude that we're in the solution equivalent of Sakaue's Regime IV (see Fig. 2.6 in the background chapter), and also the semiflexible polymer equivalent of Daoud's Region D (Fig. 2.7 in the background chapter). Only at concentrations very close to overlap concentration does the mean-field theory stop applying to our experimental data, which indicate transition to a different scaling regime.

Finding that a mean field type of scaling holds at high enough concentration, instead of a fluctuating semidilute scaling, is a first step towards trying to model the behaviour of DNA and other semiflexible polymers in confinement. This result advances fundamental knowledge in the field of polymer physics, and will also be useful in designing next generation micro/nanofluidic devices that manipulate polymers. By knowing how to model semifleixble polymer solutions in confinement, devices can be made to improve polymer flow and reduce "clogging".

60 Outlook

4.2 Outlook

While probing more confinement regimes for semiflexible polymer solutions is important, the future work of our experimental group is focused on studying the interaction between polymer molecules for now, which is also a natural extension of the work in the current thesis. Future experiment include (but are not limited to) the equilibrium behaviour of two differentially stained polymer chains confined inside a nanocavity that has been sealed from the top by a pneumatically actuated membrane; the effect of the eccentricity of the said nanocavity on the behaviour of the confined molecules; steady-state behaviour of two differentially stained chains confined in a nanochannel; steady-state behaviour of a single differentially stained molecule in a large packing of molecules, either in a slit or channel geometry. Studying interactions between molecules opens up a whole new range of physical behaviour to explore.

The next project of the author of this thesis will be studying the mixing and segregation of two nanochannel confined DNA molecules. The experimental device will be essentially the same as the one used in this thesis, except for the dimensions (it will feature nanochannels instead of nanoslits). The theory also features the use of the Onsager variational principle and a Rayleighian, but applied to the two chain system which we model as an osmotic cell with movable parition. We hope this formalism can explain behaviour we observe in our preliminary data: the tendency for both chains to never overlap inside the same section of the nanochannel at low solvent flow (segregation), the presence of a section with overlap at higher solvent flow (mixing), and the tendency for this section to form due to the counterintuitive propagation of the chain closer to the barrier back against the solvent flow into the other chain (backpropagation).

References

- [1] T. M. Birshtein. "Diagram of State for a Solution of Semirigid Macromolecules". In: *Polymer Science U.S.S.R.* 24 (1982), p. 2416.
- [2] R. Bruinsma et al. "Chromatin Hydrodynamics". In: *Biophysical Journal* 106 (2014), p. 1871.
- [3] X. Capaldi et al. "Probing the Organization and Dynamics of two DNA Chains Trapped in a Nanofluidic Cavity". In: *Soft Matter* 14 (2018), p. 8411.
- [4] L. Dai, J. R. C. van der Maarel, and P. S. Doyle. "Extended de Gennes Regime of DNA Confined in a Nanochannel". In: *Macromolecules* 47 (2014), p. 2445.
- [5] L. Dai et al. "A Systematic Study of DNA Conformation in Slitlike Confinement". In: *Soft Matter* 8 (2012), p. 2792.
- [6] M. Daoud and P. G. de Gennes. "Statistics of Macromolecular Solutions Trapped in Small Pores". In: *Journal de Physique* 38 (1977), p. 85.
- [7] M. Doi. "Onsager's variational principle in soft matter". In: *Journal of Physics: Condensed Matter* 23 (2011), p. 284118.
- [8] M. Doi. Soft-Matter Physics. Oxford University Press, 2013.
- [9] M. Doi and S. F. Edwards. *The Theory of Polymer Dynamics*. Oxford University Press, UK, 1986.
- [10] M. Doi and A. Onuki. "Dynamic Coupling Between Stress and Composition in Polymer Solutions and Blends". In: *Journal de Physique II* 2 (1992), p. 1631.
- [11] P. G. de Gennes. *Scaling Concepts in Polymer Physics*. Cornell University Press Ithaca, NY, 1979.
- [12] M. D. Graham. "Fluid Dynamics of Dissolved Polymer Molecules in Confined Geometries". In: *Annual Review of Fluid Mechanics* 43 (2011), p. 273.

62 REFERENCES

[13] J. Han, S. W. Turner, and H. G. Craighead. "Entropic Trapping and Escape of Long DNA Molecules at Submicron Size Constriction". In: *Phys. Rev. Lett.* 83 (1999), p. 1688.

- [14] A. Huang, W. Reisner, and A. Bhattacharya. "Dynamics of DNA Squeezed Inside a Nanochannel via a Sliding Gasket". In: *Polymers* 8 (2016), p. 352.
- [15] R. Hunsperger. *Integrated Optics*. Springer Berlin, Germany, 2009.
- [16] S. Jun, A. Arnold, and B.-Y. Ha. "Confined Space and Effective Interactions of Multiple Self-Avoiding Chains". In: *Phys. Rev. Lett.* 98 (2007), p. 128303.
- [17] A. Khorshid et al. "Dynamic Compression of Single Nanochannel Confined DNA via a Nanodozer Assay". In: *Phys. Rev. Lett.* 113 (2014), p. 268104.
- [18] A. Khorshid et al. "Non-Equilibrium Dynamics of Nanochannel Confined DNA". In: *Macromolecules* 49 (2016), p. 1933.
- [19] Ahmed Khorshid. "Optical Nanodozers Probing Single-DNA-Molecule Conformation and Confinement Free Energy in Cavities of Adjustable Nanoscale Dimension". Master's thesis. McGill University, 2013.
- [20] A. R. Klotz et al. "Correlated Fluctuations of DNA between Nanofluidic Entropic Traps". In: *Macromolecules* 48 (2015), p. 4742.
- [21] A. R. Klotz et al. "Measuring the Confinement Free Energy and Effective Width of Single Polymer Chains via Single-Molecule Tetris". In: *Macromolecules* 48 (2015), p. 5028.
- [22] J. Lal, S. K. Sinha, and L. Auvray. "Structure of Polymer Chains Confined in Vycor". In: *Journal de Physique II* 7 (1997), p. 1597.
- [23] T. E. Lam et al. "Genome Mapping on Nanochannel Arrays for Structural Variation Analysis and Sequence Assembly". In: *Nat. Biotech.* 30 (2012), p. 771.
- [24] E. Lundh, C. J. Pethick, and H. Smith. "Zero-Temperature Properties of a Trapped Bose-Condensed Gas: Beyond the Thomas-Fermi Approximation". In: *Phys. Rev. A* 55 (1997), p. 2126.
- [25] Y. Qi et al. "Compression of Nanoslit Confined Polymer Solutions". In: *Macromolecules* 51 (2018), p. 617.
- [26] W. Reisner, J. N. Pedersen, and R. H. Austin. "DNA Confinement in Nanochannels: Physics and Biological Applications". In: *Rep. Prog. Phys.* 75 (2012), p. 106601.
- [27] W. Reisner et al. "Directed Self-Organization of Single DNA Molecules in a Nanoslit via Embedded Nanopit Arrays". In: *Proc. Natl. Acad. Sci. U.S.A.* 106 (2009), p. 79.

REFERENCES

[28] W. Reisner et al. "Single-Molecule Denaturation Mapping of DNA in Nanofluidic Channels". In: *Proc. Natl. Acad. Sci. U.S.A.* 107 (2010), p. 13294.

- [29] W. Reisner et al. "Statics and Dynamics of Single DNA Molecules Confined in Nanochannels". In: *Phys. Rev. Lett.* 94 (2005), p. 196101.
- [30] T. Sakaue. "Semiflexible Polymer Confined in Closed Spaces". In: *Macromolecules* 40 (2007), p. 5206.
- [31] T. Sakaue and I. E. Raphaël. "Polymer Chains in Confined Spaces and Flow-Injection Problems: Some Remarks". In: *Macromolecules* 39 (2006), p. 2621.
- [32] D. W. Schaefer, J. F. Joanny, and P. Pincus. "Dynamics of Semifexible Polymers in Solution". In: *Macromolecules* 13 (1980), p. 1280.
- [33] I. Selesnick. Least square deconvolution. http://eeweb.poly.edu/iselesni/lecture_notes/least_squares/LeastSquares_SPdemos/deconvolution/html/deconv_demo.html. Accessed: 2018-11-15.
- [34] D. Stein et al. "Pressure-Driven Transport of Confined DNA Polymers in Fluidic Channels". In: *Proc. Natl. Acad. Sci. U.S.A.* 3 (2006), p. 15853.
- [35] I. Teraoka and Y. Wang. "Computer Simulation Studies on Overlapping Polymer Chains Confined in Narrow Channels". In: *Polymer* 45 (2004), p. 3835.
- [36] Y. Wang, D. R. Tree, and K. D. Dorfman. "Simulation of DNA Extension in Nanochannels". In: *Macromolecules* 44 (2011), p. 6594.
- [37] T. Wilson and C. Sheppard. *Theory and Practice of Scanning Optical Microscopy*. Academic Press London, UK, 1984.
- [38] Yuning Zhang and Walter Reisner. "Fabrication and Characterization of Nanopore-Interfaced Nanochannel Devices". In: *Nanotechnology* 26.45 (Oct. 2015), p. 455301.
- [39] J. Zhou et al. "Enhanced Nanochannel Translocation and Localization of Genomic DNA Molecules Using Three-Dimensional Nanofunnels". In: *Nature Communications* 8 (2017), p. 807.